

Article

Not peer-reviewed version

Study of Supercritical CO₂ Pipeline Flow Leaks: Effect of Equation of State, Impurity, and Outlet Diameter

Krishna Kant , [Chaouki Habchi](#) * , [Martha Hajiw-Riberaud](#) , Al-Hassan Afailal , Jean-Charles de Hemptinne

Posted Date: 3 March 2026

doi: 10.20944/preprints202603.0215.v1

Keywords: CCUS; supercritical CO₂; Impurity; pipeline leaks; depressurization; phase transition; real-fluid model (RFM)



Preprints.org is a free multidisciplinary platform providing preprint service that is dedicated to making early versions of research outputs permanently available and citable. Preprints posted at Preprints.org appear in Web of Science, Crossref, Google Scholar, Scilit, Europe PMC.

Copyright: This open access article is published under a [Creative Commons CC BY 4.0 license](#), which permit the free download, distribution, and reuse, provided that the author and preprint are cited in any reuse.

Disclaimer/Publisher's Note: The statements, opinions, and data contained in all publications are solely those of the individual author(s) and contributor(s) and not of MDPI and/or the editor(s). MDPI and/or the editor(s) disclaim responsibility for any injury to people or property resulting from any ideas, methods, instructions, or products referred to in the content.

Article

Study of Supercritical CO₂ Pipeline Flow Leaks: Effect of Equation of State, Impurity, and Outlet Diameter

Krishna Kant , Chaouki Habchi * , Martha Hajiw-Riberaud, Al-Hassan Afailal and Jean-Charles de Hemptinne

IFP Energies Nouvelles, Institut Carnot Transports Energies, 1 et 4 Avenue de Bois-Préau, 92852 Rueil-Malmaison, France

* Correspondence: chaouki.habchi@ifpen.fr

Abstract

The global urgency to mitigate climate change has intensified the development of Carbon Capture, Utilization and Storage (CCUS) technologies. A critical step in CCUS is the safe and efficient pipeline transport of supercritical CO₂ (sCO₂), where flow dynamics are strongly influenced by phase change phenomena under transient heat transfer or depressurization conditions. Indeed, pressure disturbances, such as leaks or rapid decompression events, can induce vaporization and condensation, processes further complicated by the inevitable presence of impurities (e.g., N₂, CH₄, Ar) originating from different conditions at sources. These impurities not only shift thermodynamic boundaries but also alter the kinetics of phase transitions, directly impacting pipeline safety and design. In this study, we investigate the effect of impurities on leakage mass flow rate, and decompression waves in sCO₂ pipeline transport through computational fluid dynamics (CFD) simulations, benchmarked against experimental data. A real-fluid model (RFM) implemented in the CONVERGE CFD solver is employed for these two-phase simulations, where a tabulation-based approach ensures accurate representation of thermodynamic and transport properties across multiphase regimes. Simulations are performed for varying impurity concentrations, enabling systematic evaluation of their influence on flow rate, and decompression wave propagation and associated flow variables, such as temperature. The results demonstrate strong agreement with experimental observations while providing insights into impurity-driven phase change behavior. The study investigates the effect of outlet geometry, dimensions, and role of Equation of State as well. CPA shows a better fit to the experimental results compared to PR and PC-SAFT for the simulations of supercritical CO₂. It is found that for nozzle geometry where there is smooth change in cross-section area, the simulations prediction were quite close to experiment. However, for the case of orifice venting where there is sharp change in cross-section area, the simulations under predict the leakage mass flow rate, implying the influence of head loss due to geometry. Finally, the feasibility of simulating a 50 km industrial pipeline transporting sCO₂ was investigated. The role of venting towers and gravity prove to be predominant in this specific case.

Keywords: CCUS; supercritical CO₂; Impurity; pipeline leaks; depressurization; phase transition; real-fluid model (RFM)

1. Introduction

The past decade has witnessed a significant expansion of CO₂ pipeline networks globally, driven by the growing emphasis on carbon capture, utilization, and storage (CCUS) initiatives, application in enhanced oil recovery (EOR), and to reduce anthropogenic CO₂ emissions and meet global decarbonization targets ([1,2]). Recently, significant progress has been made in CCUS technologies ([3–5]) and it has been found that the systems perform efficiently when the fluid (CO₂) is in supercritical state (sCO₂). The accurate modeling of supercritical carbon-dioxide sCO₂ transport thus becomes increasingly important for the design, safety assessment, cost reduction, and operational reliability of pipeline and storage systems in CCUS ([6–8]). One of the critical question in the safety assessment of

$s\text{CO}_2$ transport systems is the mass flow rate during depressurization or leakage, which is strongly influenced by decompression wave speed and mixture impurities. Non-equilibrium phase change retarded by nucleation and vapor-front dynamics is found to have significant effects, but only during the leakage early stage (few milliseconds) [9–11]. Consequently, metastability phenomena (i.e. non-equilibrium thermodynamics) are neglected in this article, as we intend to perform CFD simulations over significantly longer periods of time. Early work by Mahgerefteh et al. ([12]) employed 1-D models to investigate the influence of friction, heat transfer, and stream impurities on decompression wave speeds in $s\text{CO}_2$ pipelines. Subsequent studies by Woolley et al. ([6,13,14]) combined experimental and numerical approaches to analyze multi-component CO_2 mixtures, providing foundational data for safety guidelines. The recent reviews [15–18] discuss the works and challenges in accurate modeling of the decompression wave, the thermophysical properties, phase equilibria, and dispersion of CO_2 and its mixtures. Shuaiwei et al. [19] showed that isentropic assumption during depressurization predicts the decompression wave speed for CO_2 and its mixtures quite accurately. Similarly, Magen et al. [20] assuming isentropic phase change provided formulation for predicting onset of nucleation by estimating the minimum depressurization rate near the spinodal limit. Xiaoqiang et al. [21] using their experimental data correlated non-dimensional depressurization rate and degree of superheat. Liao et al. [22] analyzed the critical mass flux and decompression wave speed for CO_2 and its mixtures through 1-D analysis using different models and provided a correlation for the mass flow rate. Cao et al. [23] focused on the flow field on cross section of pipes and describe the stratification of phases during pressure leak. Hansen et al. [24,25] analyzed the problem on a vertical pipe duct and estimated reference data for 1-D phase transition model. Bhuvanker et al. [26] studied the effect of heat transfer and gravity in CO_2 blowout. Yin et al. [27] studied the depressurization phenomenon numerically using a homogeneous equilibrium model (HEM) and a homogeneous relaxation model (HRM). Log et al. [28] and Wang et al. [29] proposed correlations for the HRM relaxation time based on initial entropy. Log et al. [30] proposed a model to include the effect of the nucleation and bubble growth into the source for mass transfer. Munkejord et al. [31] and Yu et al. [32] studied the effect of impurities for $\text{CO}_2 - \text{N}_2$ mixture. Zhu et al. [33] analyzed the effect of water hammering on phase transition for the pipeline transport. Lio et al [34] proposed a neural network model to predict critical mass flow. Yu et al [35] studied the depressurization phenomenon during multistage throttling. While the previous research discussed were conducted for pressure puncture, many research were also done on orifices leakage. Ding et al. [36] proposed a pressure correction for estimating corrected leakage rate. Zhang et al. [37] analyzed the near field characteristics for $s\text{CO}_2$ during pressure leak and proposed an empirical correlation of saturation pressure P_{sat} for numerical modeling. Yu et al. [38] studied the temperature distribution and CO_2 dispersion for a pipe leak buried in soil. Similarly, in [39] they analyzed the problem numerically using leakage and seepage diffusion model. Chen et. al. [40] analyzed the effect of orifice diameter, similarly Hu et al. [41] analyzed the effect of orifice diameter for underwater pipeline leakage.

The numerical modeling of operations close to the supercritical state poses a number of challenges. Firstly, the non-linear behavior of thermodynamic and transport properties ([17,32]) near the critical point. Further complicating factor is the presence of impurities such as H_2O , N_2 , H_2 , CH_4 , O_2 , H_2S , SO_x , and NO_x , which significantly alter mixture thermodynamics and transport properties. Pure CO_2 can be accurately modeled using multi-parameter equations of state (EoS) like Span and Wagner ([42]), but it is computationally expensive. Nazeri et al. ([43]) demonstrated that incorporating a volume correction term into the Soave-Redlich-Kwong (SRK) EoS enhances density predictions for CO_2 -rich mixtures. Similarly, Demetriades et al. ([44]) derived a pressure-explicit EoS for $\text{CO}_2 - \text{N}_2 - \text{O}_2 - \text{H}_2$ systems, which outperformed the GERG-2008 model ([45]) in certain regimes. Petropoulou et al. ([46]) further compared various EoS with Universal Mixing Rules (UMR) for CO_2/CH_4 mixtures, finding that the Peng-Robinson (PR) UMR EoS provided the best vapor-liquid equilibrium (VLE) predictions. Similarly, Li and Yan [47] analyzed five different cubic EoS for VLE calculations of CO_2 and CO_2 mixtures. Diamantonis et al. [48] compared SAFT and PC-SAFT [49] with cubic EoS for

VLE modeling of CO_2 mixtures. Avendano et al. [50] has presented a parameter set for the SAFT- γ model [51] for CO_2 . Accurate prediction of transport properties (e.g., viscosity, thermal conductivity) remains another key hurdle. While empirical correlations like those of Bahadori and Vuthaluru ([52]) and Nazeri et al. ([53]) have improved viscosity estimates for CO_2 -rich mixtures, thermal conductivity modeling relies heavily on correlations such as those by Jarrahan and Heidaryan ([54]) and Rostami et al. ([55]). Cross-property interactions, such as those studied by Hellmann et al. ([56]) using the classical trajectory method, further complicate the picture. A persistent challenge is the scarcity of high-quality experimental data ([57]), which limits the validation and refinement of these models. The nonlinearities introduced by real-fluid EoS, and phase change phenomenon increases the numerical stiffness of the system as well. This severely affects the stability and convergence of solvers, consequently raising the computational cost. Modeling of formation of dry ice, which is very common for the case of $s\text{CO}_2$ depressurization is another challenge. An accurate EoS model of solid CO_2 is needed. Trusler ([58,59]) and Jager and Span ([60]) proposed a Helmholtz and Gibbs energy based model for solid CO_2 , respectively. These models have been validated for various systems ([61–63]) and found to be reasonably accurate with experiment. Maltby ([64]) reviewed various experimental data for various CO_2 systems and found out the deviation is minimum with PR EoS considering overall range of various conditions. Bhatia et al. ([65]) found that CPA outperforms PR for the case of condensation of CO_2 through convergent-divergent nozzle.

Despite the substantial body of work summarized above, several important limitations remain. Most existing investigations rely predominantly on one-dimensional homogeneous equilibrium or relaxation models to predict decompression wave speeds and critical mass flux. While these approaches provide valuable theoretical insight and are computationally efficient, they inherently neglect multi-dimensional flow structures, spatial phase stratification, and local non-uniformity that arise during realistic pipeline leakage. Furthermore, many studies emphasize either thermodynamic modeling or empirical correlations independently, with limited integration into fully coupled CFD frameworks capable of resolving transient flow–thermodynamics interactions over engineering time scales. In addition, although the influence of impurities has been recognized, a systematic numerical investigations incorporating real-fluid equations of state together with transport-property variations remain scarce. The combined effects of non-linear thermophysical behavior near the critical region, phase change, and stiff source terms pose significant challenges for stable and efficient numerical solvers, which has limited the application of high-fidelity CFD to practical large-scale problems. Consequently, there is still a lack of robust, computationally tractable models that can accurately predict depressurization dynamics and mass discharge rates for realistic multi-component CO_2 mixtures over extended transient periods relevant to safety assessment and pipeline design. The present work aims to address these gaps by developing and applying a CFD-based framework that incorporates real-fluid thermodynamics, mixture-dependent properties, and transient multiphase effects to systematically evaluate decompression behavior and leakage characteristics of CO_2 pipelines under practical operating conditions. In the present work, a high-fidelity Real Fluid Method (RFM) solver implemented on CONVERGE CFD v4.1 is used. The framework is validated for real-gas evaporating and non-evaporating sprays [66–68]. The thermophysical properties are calculated by a robust thermodynamic solver developed at IFP Energies Nouvelle [69]. Model validation leverages high-resolution experimental pressure–temperature data from Munkejord et al. [31,70,71], providing a rigorous benchmark for assessing accuracy. The selected binary systems are $\text{CO}_2 - \text{N}_2$, $\text{CO}_2 - \text{CH}_4$, and $\text{CO}_2 - \text{Ar}$ representing the major non-condensable impurities relevant to current and emerging $s\text{CO}_2$ capture, transport, and storage applications [72]. The key contributions of this work are:

1. A critical assessment of the influence of the equation of state on the prediction of thermophysical properties for supercritical CO_2 and its mixtures,
2. CO_2 rich mixtures depressurization analysis of the flow rate, and pressure depression and void fraction profiles with different outlet diameters and geometries,

- An evaluation of the effect of impurities by simulating binary mixture on the decompression wave propagation and the resulting critical mass flow rate.

The following sections detail the numerical methodology (section 2) and computational setup and mesh sensitivity study (section 3). Results and discussions (section 4) include the validation of CPA EoS and VLE thermodynamic equilibrium. Effect of impurities is studied in detail for various parameters of concern in pipeline industry. Section (4) also compare simulated pressure profile, gas fraction variations, and thermodynamic path against experimental benchmarks. Effect of impurities on decompression wave speed, mass flow rate and Mach number are also discussed. Finally, the conclusion discusses key findings and highlights the broader implications of impurity-sensitive modeling for the design and transient safety assessment of industrial-scale sCO₂ transport systems.

2. Numerical Methodology

2.1. Governing Equations

The mixture is represented as a single effective fluid in which both phases share identical velocity, pressure, and temperature fields. Accordingly, the formulation reduces to four governing equations [73–76]:

$$\frac{\partial \rho}{\partial t} + \frac{\partial \rho u_i}{\partial x_i} = 0 \quad (1)$$

$$\frac{\partial \rho u_i}{\partial t} + \frac{\partial \rho u_i u_j}{\partial x_j} = -\frac{\partial P}{\partial x_i} + \frac{\partial}{\partial x_j} (\tau_{ij} + \tau_{ij}^{SGS}) \quad (2)$$

$$\frac{\partial \rho e}{\partial t} + \frac{\partial \rho e u_j}{\partial x_j} = -P \frac{\partial u_j}{\partial x_j} + (\tau_{ij} + \tau_{ij}^{SGS}) \frac{\partial u_i}{\partial x_j} + \frac{\partial}{\partial x_j} (q_j + q_j^{SGS}) \quad (3)$$

$$\frac{\partial \rho Y_k}{\partial t} + \frac{\partial \rho Y_k u_j}{\partial x_j} = -\frac{\partial}{\partial x_j} (J_{kj} + J_{kj}^{SGS}) \quad (4)$$

Here, ρ , u , P , T , and e denote the mixture density, velocity, pressure, temperature, and specific internal energy. The molecular viscous stress tensor is given by

$$\tau_{ij} = \mu \left(\frac{\partial u_i}{\partial x_j} + \frac{\partial u_j}{\partial x_i} - \frac{2}{3} \frac{\partial u_k}{\partial x_k} \delta_{ij} \right) \quad (5)$$

with δ_{ij} the Kronecker delta.

The heat flux and diffusive flux of species are expressed as

$$q_j = -\lambda \frac{\partial T}{\partial x_j} + \sum_m J_{mj} h_m, \quad J_{mj} = -\rho D_m \frac{\partial Y_m}{\partial x_j} \quad (6)$$

where h_m is the species enthalpy, D_m the molecular diffusivity, and Y_m the mass fraction of species m . The transport coefficients μ and λ are obtained from the correlations of Chung et al. [77].

The sub-grid scale (SGS) stresses and fluxes are modeled by analogy with molecular terms. The SGS stress tensor is

$$\tau_{ij}^{SGS} = \frac{\mu^{SGS}}{\mu} \tau_{ij} \quad (7)$$

while the turbulent contributions to heat and mass transfer are

$$q_j^{SGS} = -\lambda_t \frac{\partial T}{\partial x_j} + \sum_m J_{mj}^{SGS} h_m, \quad J_{mj}^{SGS} = -\rho D_{mt} \frac{\partial Y_m}{\partial x_j} \quad (8)$$

The turbulent transport properties are modeled through

$$D_{mt} = \frac{\mu^{SGS}}{\rho Sc_t}, \quad \lambda_t = \frac{C_p \mu^{SGS}}{Pr_t} \quad (9)$$

with $Sc_t = 0.7$, $Pr_t = 0.9$, and C_p the specific heat at constant pressure. The eddy viscosity μ_{SGS} follows the σ -model [78],

$$\mu_{SGS} = \rho(C\Delta)^2\delta \quad (10)$$

where $C = 1.5$, $\Delta = V^{1/3}$, V being the grid-cell volume, and $\delta = \frac{\sigma_3(\sigma_1 - \sigma_2)(\sigma_2 - \sigma_3)}{\sigma_1^2}$ using the singular values σ_i of the resolved velocity-gradient tensor. In this work, cross-coupling effects such as Soret and Dufour are neglected.

2.2. Thermodynamic Modeling

The Real-Fluid Method (RFM) [73–76] is based on tabulated thermodynamic data generated using the IFPEN-Carnot library [69]. The library applies PT-flash calculations for mixtures and PH-flash for pure fluids, with different cubic and association EoS (PR [79], CPA [80], PC-SAFT [49]). Flashing involves a stability test (tangent-plane distance criterion) followed by phase-split determination.

The lookup tables, discretized in (T, P, Y_k) for mixtures (or (h, P) for pure fluids), provide equilibrium density, internal energy, vapor fraction, heat capacity, sound speed, and transport properties. Property queries are interpolated via Inverse Distance Weighting (IDW) [81]. This methodology has been successfully applied to binary [66,68,82] and ternary [67] mixtures and is implemented in CONVERGE CFD [83].

The tables are used during the runtime for:

- Property evaluation as function $f(T, P, Y_k)$,
- Reverse lookup $T = f(e, P, Y_k)$ after solving for internal energy.

Because of the non-linear behavior of real-fluid EoS, the standard pressure equation must be reformulated. A pressure-density ratio is defined locally at each cell and time step to incorporate the effects of real fluid compressibility as

$$\phi^* = \left(\frac{\partial \rho}{\partial p} \right)_{T,Y} \quad (11)$$

Within the PISO loop, the pressure equation reads:

$$\frac{\partial^2 (P^{**} - P^*)}{\partial x_i \partial x_i} - \frac{\phi^* (P^{**} - P^*)}{dt^2} = \frac{(\rho^{EoS^*} - \rho^n)}{dt^2} + \frac{1}{dt} \left(\frac{\partial \rho^* u_i^{**}}{\partial x_i} - S \right) \quad (12)$$

Here $**$ and $*$ refer to successive PISO iterations, EoS designate the density obtained from the table, and n indicates the current time step. Although no explicit phase-change source terms are included in the transport equations under equilibrium, mass and energy transfer are consistently handled via property lookup and reverse-lookup procedures. A similar procedure is used for single component CO_2 simulations where the table inputs are (h, P) . In this case, h is evaluated as $(e + P/\rho)$ and the temperature is among the output in the table.

2.3. Numerical Schemes

The spatial discretization is first-order accurate with a first-order Euler upwind scheme. Time integration is performed using a first-order explicit Euler forward scheme. This treatment enhances numerical robustness during the highly transient depressurization phase while maintaining computational efficiency. A dynamically adaptive time-stepping strategy is adopted. During the initial stage of depressurization, where the flow is strongly shock-dominated and characterized by steep pressure gradients, the time step is on the order of $\mathcal{O}(10 \text{ ns})$. As the flow transitions beyond the choked regime and pressure gradients relax, the time step is gradually increased up to $\mathcal{O}(10 \text{ ms})$. Numerical stability is primarily governed by shock propagation and rapid pressure-wave dynamics. The maximum allowable time step is controlled using a Courant–Friedrichs–Lewy (CFL) criterion based on the local Mach number. The maximum CFL number attained at maximum dt is 2.0 for laboratory-scale pipeline simulations and 8.0 for industrial-scale pipeline configurations. The larger permissible CFL number in industrial-scale cases is attributed to the longer characteristic length scales and comparatively smoother

spatial gradients following the initial decompression front propagation. All simulations are performed on AMD EPYC Genoa 9534 processors operating at 2.45 GHz on the ORION super-computing cluster. The number of cores used are 128 cores for lab scale pipeline flow and 256 cores for the industrial scale pipeline flow. Thermodynamic closure within the RFM framework is provided by the VTPR equation of state. Thermodynamic properties are evaluated using pre-tabulated data with a resolution of

$$\Delta T = 1 \text{ K}, \quad \Delta P = 0.1 \text{ bar}, \quad \Delta Y = \text{Impurity mass fraction.} \quad (13)$$

The selected tabulation resolution is consistent with prior validation studies ([65,68,74–76]), ensuring an appropriate balance between interpolation accuracy and computational cost for multi-component CO₂ mixture depressurization simulations.

3. Computational Setup

3.1. Setup Description

The computational domain is shown in Figure 1. It is a cylindrical pipe of diameter $D = 40.8$ mm and length $L = 61.7$ m, relevant to the experimental setup of Munkejord et al. [31,70]. The domain has two boundaries. First, at left side is the OUTLET plane which is at the location of the disk rupture (simulating the leak), and the rest of the boundary are defined as WALL. Hence, the boundary condition are Dirichlet condition for pressure and Neumann for the rest of the depending variables such as temperature and Velocity at outlet. The outlet pressure is defined by the atmospheric condition with total pressure as 1 atm. At the Wall, no slip condition is imposed. The temperature is assumed to remain constant at the wall throughout the simulation i.e. $T_{wall} = T_0 = 298\text{K}$. The pipe is initially filled with supercritical CO₂, as the initial condition inside the pipeline is defined by the fluid thermodynamic state ($T_0 = 298\text{K}$) and ($P_0 = 12.27\text{MPa}$) which is greater than the critical pressure ($P_c = 7.3773\text{MPa}$) of pure CO₂. The disk ruptures at time $t = 0$ and sCO₂ inside is exposed to atmospheric condition ($P_{amb} = 0.1\text{MPa}$, $T_{amb} = 277\text{K}$) causing a two-phase boiling shock including a sudden expansion wave with a violent phase change. The initial and atmospheric conditions remains the same for all the cases. The test matrix is designed to systematically assess the influence of the equation of state (EoS), impurities, outlet geometry and diameter. The test matrices for the present study are shown in Tables 1–3. In addition to these test cases, a reference case C0 of pure CO₂ is also studied, the initial and atmospheric conditions are similar i.e., ($P_0 = 12.22\text{MPa}$, $T_0 = 297.6\text{K}$) and ($P_{amb} = 0.1\text{MPa}$, $T_{amb} = 281\text{K}$) [70]. The geometry for the cases C10–C13 are taken from the reference [71] and are shown in Figure 1(b). The new outlet plane for these cases are at a distance $l = 50\text{mm}$ from the previous outlet plane and the boundary area is varied through d , the diameter of the orifice or nozzle. For the case of orifice a rectangular boundary is chosen instead of circular keeping the geometry and outlet boundary net area identical. Fluid impurities and initial conditions are selected to provide detailed informations relevant to IFPEN's current projects.

Table 1. Test matrix for depressurization simulations of supercritical CO₂–N₂ mixtures, highlighting the influence of equation of state (EoS).

Case ID	EoS	Outlet Type	Impurity (mol%)	Impurity (mass%)
C1(No. 9[31])	CPA	FB	N ₂ (1.8)	N ₂ (1.15)
C2(No. 9[31])	PR	FB	N ₂ (1.8)	N ₂ (1.15)
C3(No. 9[31])	SAFT	FB	N ₂ (1.8)	N ₂ (1.15)

EoS abbreviations: PR — Peng–Robinson; CPA — Cubic-Plus-Association; SAFT — Statistical Associating Fluid Theory. Outlet type abbreviations: FB — Full bore. Here, FB is with 40.8 mm diameter.

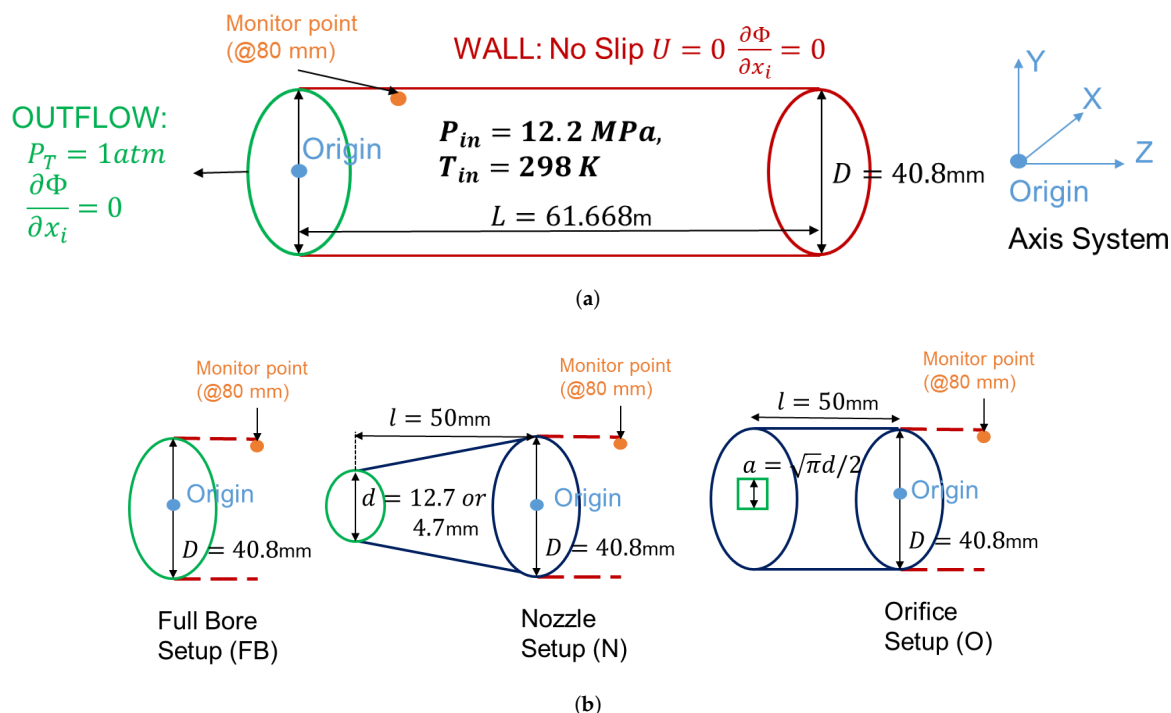


Figure 1. (a) Computational domain and boundary conditions for the lab scale CO_2 pipeline depressurization. (b) Various outlet geometries setup used in the present study. Green lines shows the outflow plane. P_T is the specified total pressure at the outlet. Φ designates any dependent variables, except P .

Table 2. Test matrix for depressurization simulations of supercritical CO_2 mixtures, highlighting the influence of impurities.

Case ID	EoS	Outlet Type	Impurity (mol%)	Impurity (mass%)
C4	CPA	FB	N_2 (3.6)	N_2 (2.3)
C5	CPA	FB	N_2 (5.4)	N_2 (3.5)
C6	CPA	FB	CH_4 (3.6)	CH_4 (1.3)
C7	CPA	FB	CH_4 (5.4)	CH_4 (2.0)
C8	CPA	FB	Ar (3.6)	Ar (3.2)
C9	CPA	FB	Ar (5.4)	Ar (4.9)

EoS abbreviations: PR — Peng–Robinson; CPA — Cubic-Plus-Association; SAFT — Statistical Associating Fluid Theory. Outlet type abbreviations: FB — Full bore. Here, FB is with 40.8 mm diameter.

Table 3. Test matrix for depressurization simulations of supercritical $\text{CO}_2 + \text{N}_2$ mixture, highlighting the influence of outlet geometry and diameter.

Case ID	EoS	Outlet Type	Impurity (mol%)	Impurity (mass%)
C10(No. 13 [71])	CPA	O (12.7 mm)	N_2 (1.8)	N_2 (1.15)
C11(No. 16 [71])	CPA	O (4.5 mm)	N_2 (1.8)	N_2 (1.15)
C12(No. 18 [71])	CPA	N (12.7 mm)	N_2 (1.8)	N_2 (1.15)
C13(No. 17 [71])	CPA	N (4.5 mm)	N_2 (1.8)	N_2 (1.15)

EoS abbreviations: CPA — Cubic-Plus-Association. Outlet type abbreviations: O — Orifice; N — Nozzle.

3.2. Mesh Sensitivity

The mesh sensitivity is performed for the Case C1 in Table 1. A uniform mesh is used for all the cases in the present work, with fixed 4 cells in the cross-section, i.e. $\Delta_x = \Delta_y = 20.4$ mm, and refined in axial direction making the setup closest to 1D-setup. The mesh sensitivity is analyzed with three different mesh resolutions i.e. $L/\Delta_z = 4000, 8000, 16000$ which corresponds to $\Delta_z \approx 16, 8, 4$ mm and

approximately 14.8, 29.6, 59.2 thousands of cells. The results are analyzed through a monitor point at the distance $x = 80$ mm, as shown in Figure 1, which corresponds to the normalized distance $x/D \approx 2$. The results from grid sensitivity are depicted in Figure 2. Apart from grid sensitivity the result also validates the numerical model with experimental data. The error percentage in the pressure and gas volume fraction profile are less than 10% before the fluctuation in properties begins due to interactions with the reflected pressure waves. The computational time taken for the different mesh resolutions i.e. $L/\Delta_z = 4000, 8000, 16000$ are 3.24, 6.29, 20.7 hrs, respectively. Hence, the mesh resolution with $L/\Delta_z = 8000$ is found to be adequate for the present study.

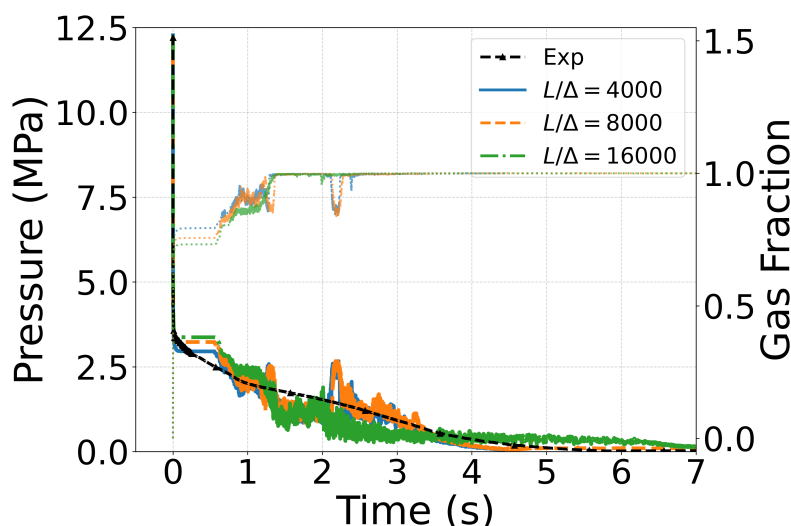


Figure 2. Pressure and gas fraction comparison at different grid resolutions $D/\Delta_z = 4000, 8000, 16000$ and experiment [31] for Case C1. Dark lines represents pressure while light lines represent gas fraction profiles.

4. Results and Discussions

Understanding the depressurization of supercritical $s\text{CO}_2$ requires capturing the interplay of thermodynamic and flow phenomena. The results are analyzed through pressure, temperature, and gas volume fraction data, the three independent thermodynamic property essential to define the thermodynamic state of the binary system. These data are also used to analyze the thermodynamic path of the system during depressurization. The decompression wave speed (u_w) represents the propagation velocity of a given pressure level P along the pipeline during depressurization. It is determined by tracking the arrival time of a specific pressure value at two axial locations. The two monitor points of choice are at $x_1 = 1.6$ m and $x_2 = 61.28$ m, giving a separation distance of $\delta x = x_2 - x_1 = 59.68$ m. For a selected pressure level P , the corresponding arrival times $t_1(P)$ and $t_2(P)$ are identified from the pressure–time histories at x_1 and x_2 , respectively. These times are defined as the instants at which the local pressure signal first reaches the given value P during depressurization. Linear interpolation between discrete data points is used to determine the arrival times. The decompression wave speed (u_w) is then computed as

$$u_w(P) = \frac{\delta x}{t_2(P) - t_1(P)}. \quad (14)$$

Thus, $u_w(P)$ represents the propagation speed of an isobaric pressure level P along the pipeline. Apart from these, mass flow rate and Mach number are also studied as these informations are crucial for the design analysis of $s\text{CO}_2$ dispersion modeling. Mass flow rate and Mach number are obtained at the outflow boundary.

4.1. Heat Transfer and Boundary Conditions

The role of heat transfer models is significant in $s\text{CO}_2$ pipeline transport. The present section compares two boundary conditions i.e. adiabatic and isothermal conditions at the wall. For isothermal,

the wall is assumed to be at the initial temperature i.e. $T_{wall} = T_0 = 298K$, throughout the observational time, i.e. 7s. From Figure 3(a),(b) and (d), the system is found to follow the same thermodynamic path, pressure and temperature profile in the initial phase (up to 1.5s) respectively, where the flow features are dominated by the initial shock wave expansion, phase change and Joule-Thompson cooling effect. Later on for the two-phase state fluid and especially when the fluid becomes gaseous, the heat transfer model starts showing major differences, as depicted in Figure 3(a) and Figure 3(c). It can be seen that a simplistic model of heat transfer that maintains the isothermal condition brought the depressurization pressure (Figure 3(b)) and temperature (Figure 3(c)) profiles close to experimental data. At adiabatic condition there is no source of heat intake into the fluid, hence the fluid pressure rapidly decays to atmospheric pressure and stays at minimum temperature obtained through Joule-Thompson cooling. Although, isothermal boundary condition is a better choice than adiabatic wall, this study shows that wall heat transfer needs to be computed accurately to capture the transition of the decompression wave speed as shown in Figure 3(c) for the various phases and the minimum temperature attained by the system as shown in Figure 3(d). However, the isothermal condition is found to follow well the behavior of the experimental data. Hence, the isothermal wall is the chosen boundary condition for further study in this work.

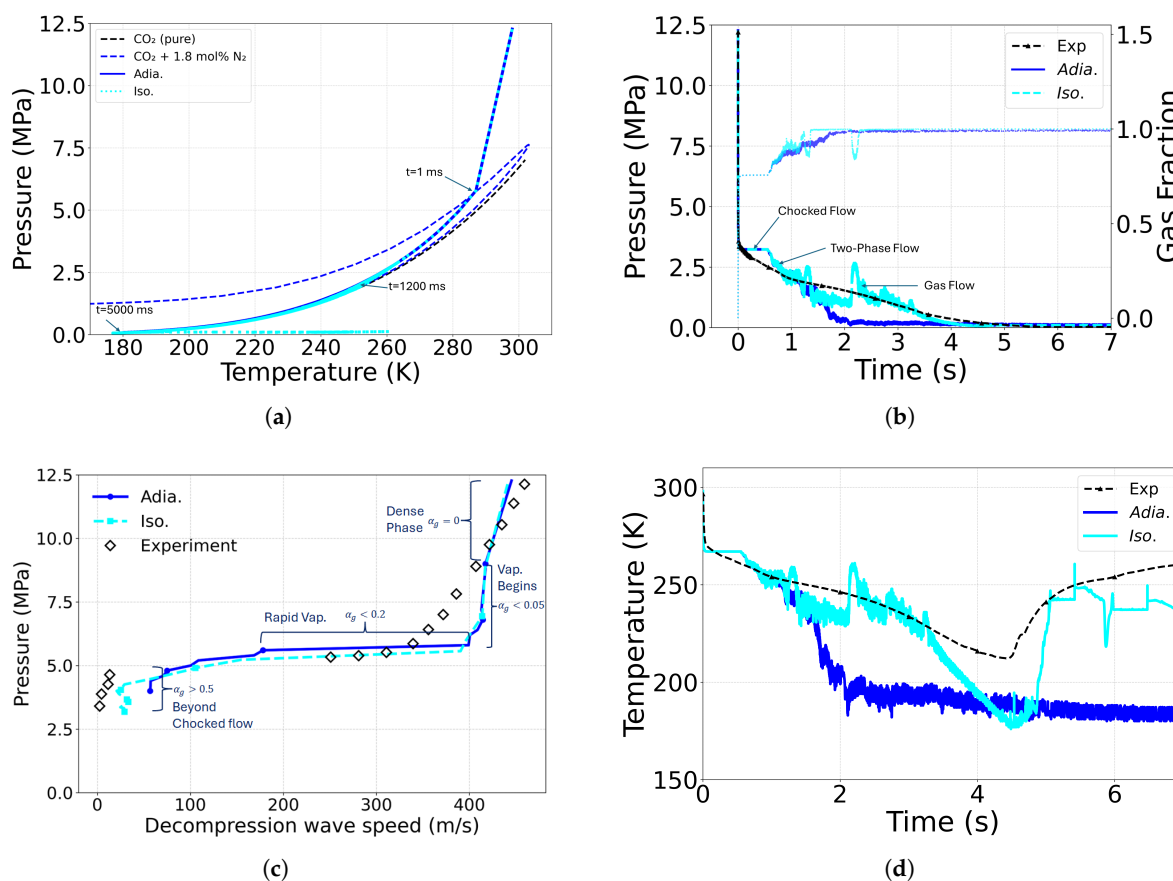


Figure 3. (a) Thermodynamic path for adiabatic and isothermal boundary conditions for case C1. (b) Pressure and gas fraction comparison at different boundary conditions for Case C1. Dark lines represents pressure while light lines represent gas fraction profiles. (c) Comparison of decompression wave speed at different boundary conditions for Case C1. (d) Temperature comparison at different boundary conditions for Case C1.

4.2. Effect of Equation of State

The cases C1–C3 in Table 1 are investigated to assess the effect of the equation of state (EoS) on the depressurization behavior of supercritical sCO₂. Three widely used EoS, namely CPA, Peng–Robinson (PR), and PC-SAFT, are considered in this study. These EoS yield slight variations in prediction of density, speed of sound, and phase equilibrium under near-critical and two-phase conditions. As

as a result, they influence key flow characteristics during depressurization, including pressure wave propagation, mass discharge rate, temperature evolution, and the onset and extent of phase change. The shape of the phase envelopes as computed from the three equations is shown in Figure 4. CPA and PC-SAFT show a larger critical temperature and pressure for the case of $\text{CO}_2 + \text{N}_2(1.8\% \text{mol})$. This also shifts the initiation point of vaporization at the bubble line (Figure 4(a)), resulting in the following order for saturation pressure: $P_{\text{satPR}} < P_{\text{satCPA}} < P_{\text{satPC-SAFT}}$ at a given temperature, while for the saturation temperature the order is: $T_{\text{satPR}} > T_{\text{satCPA}} > T_{\text{satPC-SAFT}}$ at a given pressure. Because of different bubble lines of the EoS, the flow enters the two-phase flow state somewhat later for PR in comparison to CPA and PC-SAFT (see Figure 4(a)). Hence, a delayed choked flow pressure and duration is observed for PR in comparison to CPA and PC-SAFT, as can be seen at about 1s in the pressure and temperature evolution plotted in Figure 4(b,d). For the current monitor point, the flow enters to the gaseous phase at about 2s, after two interactions with reflected pressure waves from the closed end of the pipe, which have led to more or less pressure oscillations in the two-phase flow region. The depressurization rate is different at each stage of interaction, and so is the gas fraction. The flow leaves the phase envelope, or enters the gaseous state at almost identical thermodynamic state for all EoS. Figure 4(c) shows the comparison of decompression wave speed (u_w) for various EoS, as it is highly dependent on speed of sound predicted by the EoS for a given phase and needed for ductile fracture studies, for instance. It is observed that the CPA model predicts the decompression wave speed and the transition pressure well, while the PC-SAFT over predicts the decompression wave speed and the PR over predicts the transition pressure. Hence, CPA is the chosen EoS for further studies conducted in this work.

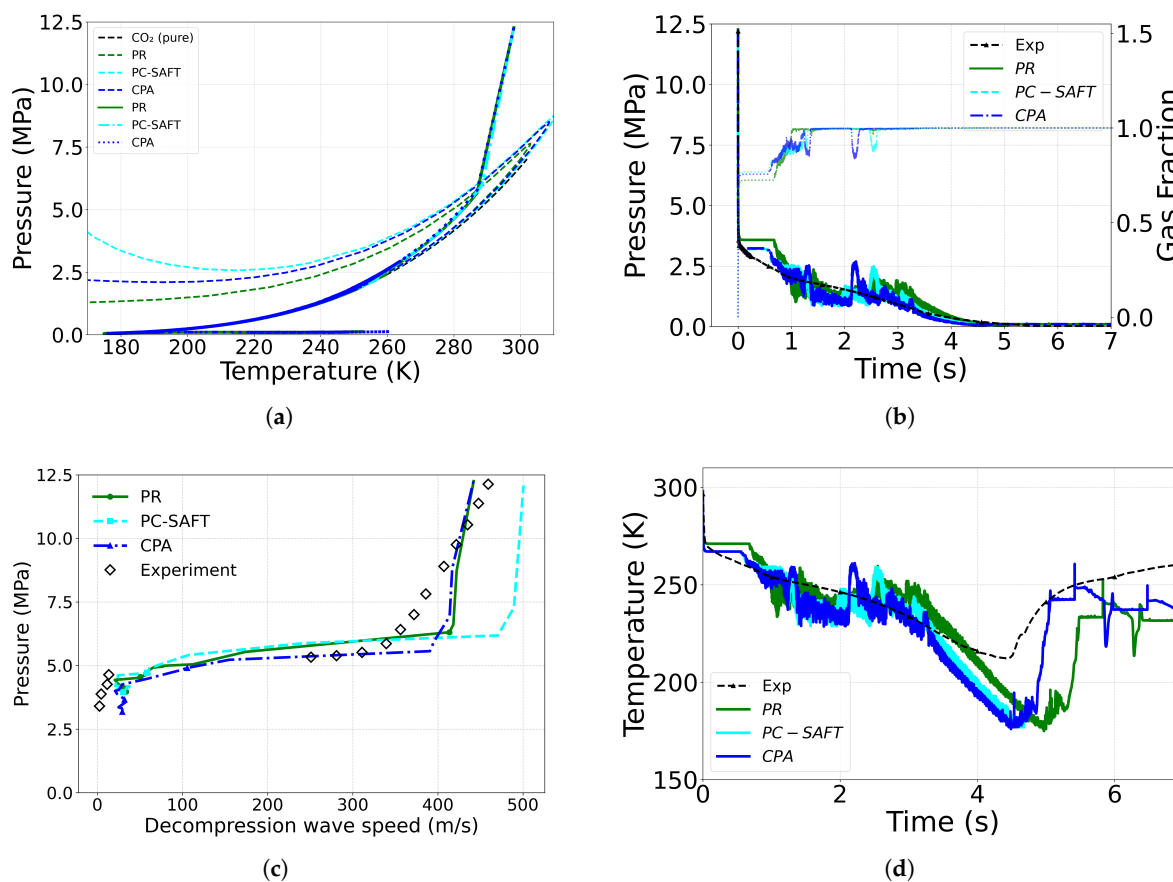


Figure 4. (a) Thermodynamic path for different equation of states for case C1. (b) Pressure and gas fraction comparison at different EoS for Case C1. Dark lines represents pressure while light lines represent gas fraction profiles. (c) Comparison of decompression wave speed (u_w) for different EoS for Case C1. (d) Temperature comparison for different EoS for Case C1.

4.3. Effect of Impurity

4.3.1. Comparison with Pure CO₂

This section compares the cases between pure CO₂ and the CO₂ + N₂(1.8%mol) mixture, i.e. cases C0 and C1 in Table 2. It should be noted that a PH-Flash algorithm is used in the IFPEN-Carnot library [69] to determine the phase transition and equilibrium condition for pure CO₂ through the generation of an appropriate table of thermodynamic properties, as discussed in Section (2.2). Figure 5 shows the comparison of thermodynamic state, pressure and gas fraction profiles, and decompression wave speed for pure and rich CO₂ mixtures. The saturation point at which the vaporization starts is well predicted for both pure CO₂ and CO₂ + N₂(1.8%mol) mixture. As shown in Figure 5(a), the depressurization rate is slightly higher for pure CO₂ in comparison to CO₂ with impurities, as the steepness and the saturation point is lower for pure CO₂. The gas volume fraction at choked flow state is also higher for pure CO₂ in comparison to rich CO₂ mixtures (Figure 5(b)). In this Figure, the two reflected pressure waves from the pipeline end can be clearly seen, without spurious oscillations induced by the impurity for the rich CO₂ mixture. In addition, the transition pressure for decompression wave speed (u_w) for pure CO₂ is smaller than with impurities, as depicted from the phase envelope as well. The thermodynamic state of entering the gaseous state is close for pure and rich CO₂ mixtures. However, the saturation pressure is slightly lower for pure CO₂, as expected (Figure 5(c)). Finally, one may note that the present simulation predicts larger choked flow state in comparison to the experiments [31,70], which could be because of the effect of venting and pipeline divergence at the outlet.

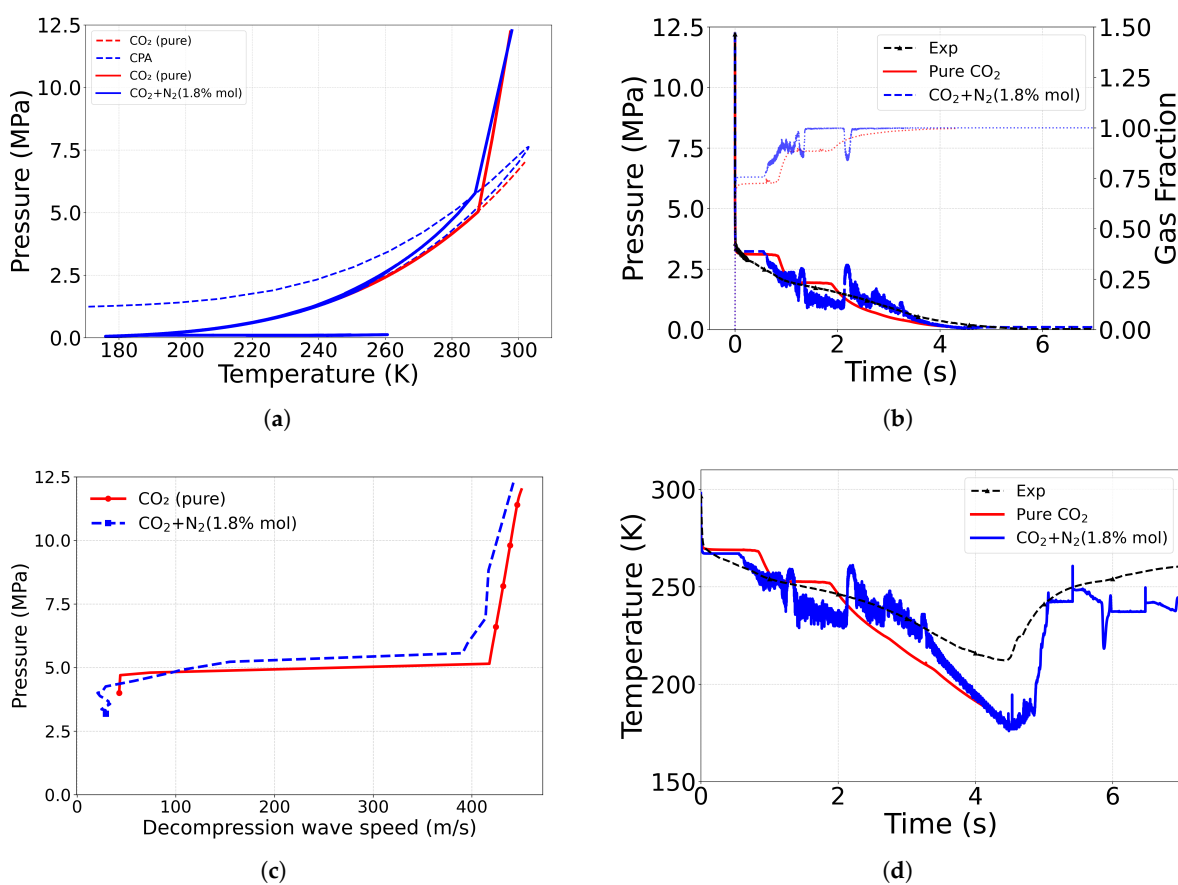


Figure 5. (a) Thermodynamic path for pure and rich CO₂ mixtures. (b) Pressure and gas fraction comparison for pure and rich CO₂ mixtures. Dark lines represents pressure while light lines represent gas fraction profiles. (c) Comparison of decompression wave speed for pure and rich CO₂ mixtures. (d) Temperature comparison for pure and rich CO₂ mixtures.

4.3.2. Comparison Between Different Impurities N_2 , CH_4 , Ar

As discussed in the introduction Section 1, the selected binary systems are $CO_2 - N_2$, $CO_2 - CH_4$, and $CO_2 - Ar$ representing the major non-condensable impurities relevant to current and emerging sCO_2 capture, transport, and storage applications [72]. The depressurization behavior of multi-component fluids is governed by a combination of thermodynamic, caloric, and transport properties, including mixture molar mass, critical properties, acentric factor, phase equilibrium characteristics, speed of sound, Joule–Thomson coefficient, and heat capacity. Figure 6 shows the comparison of thermodynamic state, pressure, gas fraction, and decompression wave speed for cases C4, C6, and C8. Since the speed of sound C_s and the critical compressibility factor Z_c are close to each other for all the mixtures at the given initial condition which is very close to critical point for supercritical flows, the depressurization rate and the pressure profile are also close to each other until the vaporization begins, as shown in Figure 6(a). Indeed the point of vaporization obviously differs for each case, but the thermodynamic state paths inside the phase envelope collapse again before the dew point and the gaseous phase, as shown also in Figure 6(a). The transition pressure of the decompression wave speed decreases in the same order $N_2 > Ar > CH_4$ than the bubble saturation point in Figure 6(c). Similarly, the decompression wave speed for the gaseous phase in the Figure 6(c) also increases in the same order $N_2 > Ar > CH_4$. Finally, changing the impurity does not induces very different results near the critical point during depressurization, although few differences in the pressure and temperature evolutions mainly during the two-phase stage, as shown in Figure 6(b,d).

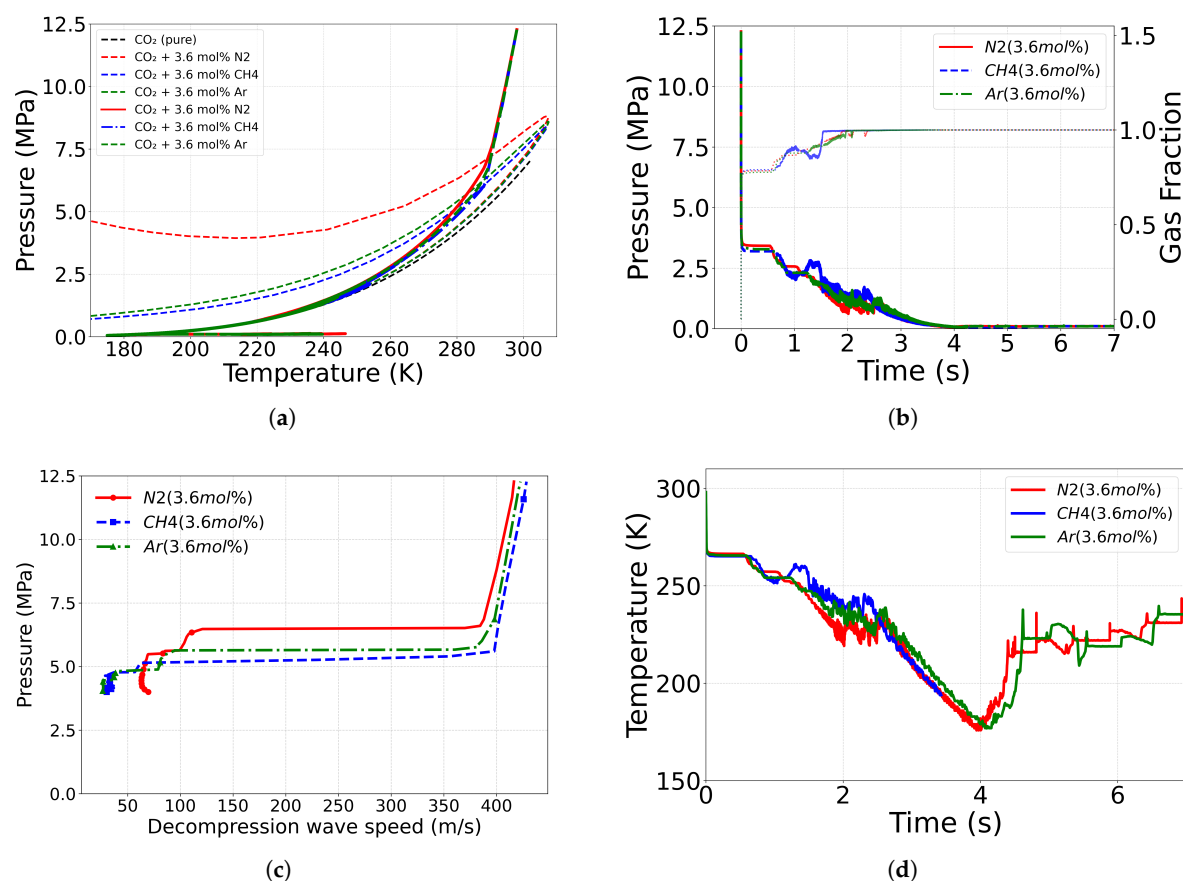


Figure 6. (a) Thermodynamic path for various CO_2 rich mixtures at 3.6% by mol concentration impurity. (b) Pressure and gas fraction comparison for various CO_2 rich mixtures at 3.6% by mol concentration impurity. Dark lines represents pressure while light lines represent gas fraction profiles. (c) Comparison of decompression wave speed for CO_2 rich mixtures at 3.6% by mol concentration impurity. (d) Temperature comparison for various CO_2 rich mixtures with 3.6% by mol concentration impurity.

4.3.3. Role of Impurity Mass Fraction

The comparison of Figure 6 and Figure 7 shows the role of the mole fraction on depressurization thermodynamic path, pressure, gas-fraction and decompression wave speed. The increase in mole fraction of impurities shifts the phase envelope upwards, accordingly shifting the onset pressure of vaporization, choked flow pressure and gas fraction. From Figure 6(c) and Figure 7(c), for low composition mixtures, the decompression wave speed in the dense phase at $t = 0$ is closer to the pure CO_2 and remains the same for all the mixtures as 410m/s . However, for higher impurities concentration, the effect of impurities on wave speed becomes visible. The decompression wave speed for dense phase decreases as: $\text{CH}_4(427\text{m/s}) < \text{Ar}(410\text{m/s}) < \text{N}_2(400\text{m/s})$. It should be noted that the minimum temperature value for the RFM tabular properties for the case of $\text{CO}_2 + \text{CH}_4$ mixtures is 190K . Hence, beyond this limit the sharp decrease in temperature is observed which is omitted from Figure 6(d) and Figure 7(d) as those are numerical artifacts induced by extrapolation of data from the out of the range of the RFM thermodynamic table. However, as shown in the pressure and gas fraction plot (Figure 6(b) and Figure 7(b)), the chosen range covers the entire two-phase transition region.

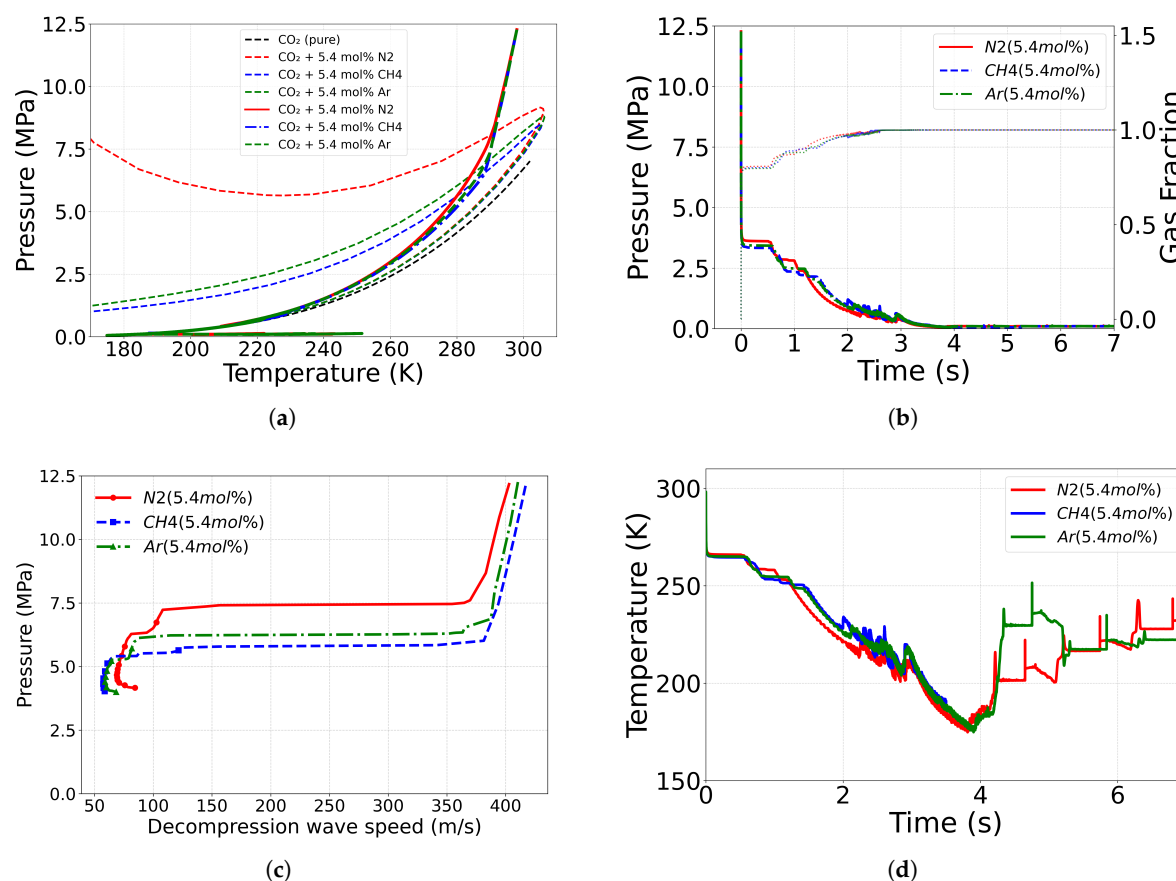


Figure 7. (a) Thermodynamic path for various CO_2 rich mixtures at 5.4% by mol concentration impurity. (b) Pressure and gas fraction comparison for various CO_2 rich mixtures at 5.4% by mol concentration impurity. Dark lines represent pressure while light lines represent gas fraction profiles. (c) Comparison of decompression wave speed for CO_2 rich mixtures at 5.4% by mol concentration impurity. (d) Temperature comparison for various CO_2 rich mixtures with 5.4% by mol concentration impurity.

4.4. Effect of Outlet Geometry and Diameter

Cases C10-C13 in Table 3 analyze the effect of outlet geometry and diameter. The minimum cross-section area in the flow circuit determines the choking mass flow rate [71]. The results presented in this section follow a similar trend as reported in the experimental work of Hammer et al. [71]. However, a slight difference in the choked flow state is expected as the present simulation is with $\text{N}_2(1.8\%$ by mol) as an impurity. Figure 8 and Figure 9 illustrate that changing mass flow rate by

changing the outlet geometry and diameter brings changes in the dense phase of the fluid, however as the vaporization begins the system follows the same thermodynamic path. The decrease in mass flow rate, reduces the rate of depressurization as shown by the pressure profile. This tends the thermodynamic path to shift right ward, representing higher density for a reduced mass flow rate. The decompression wave speed does not have a clear demarcation for the dense phase and gaseous phase for these cases as the fluid remains in the two phase state for the simulated time. Also prolonged choked flow state, brings difficulty in estimating instantaneous time for a given pressure level, and hence the difficulty in calculating accurate decompression wave speed. Hence, the decompression wave speed plot is omitted for the present section. It is also noteworthy that the simulations become numerically more unstable under choked flow conditions, thereby requiring a smaller time step (dt) to maintain stability.

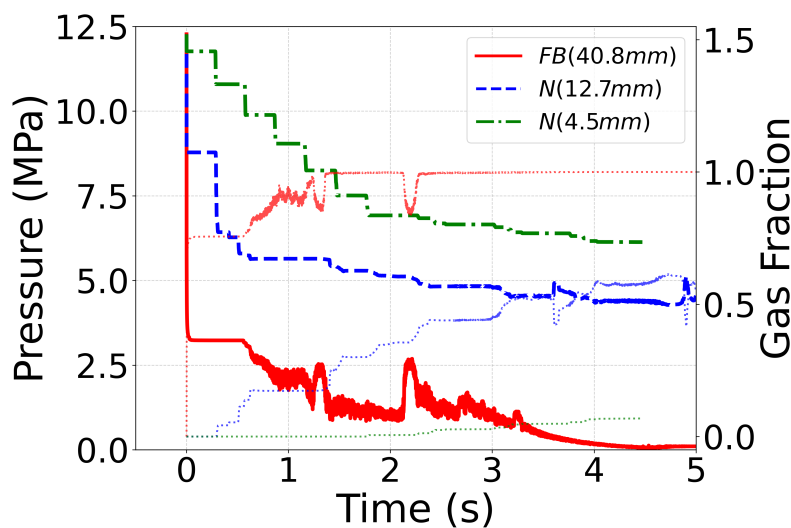
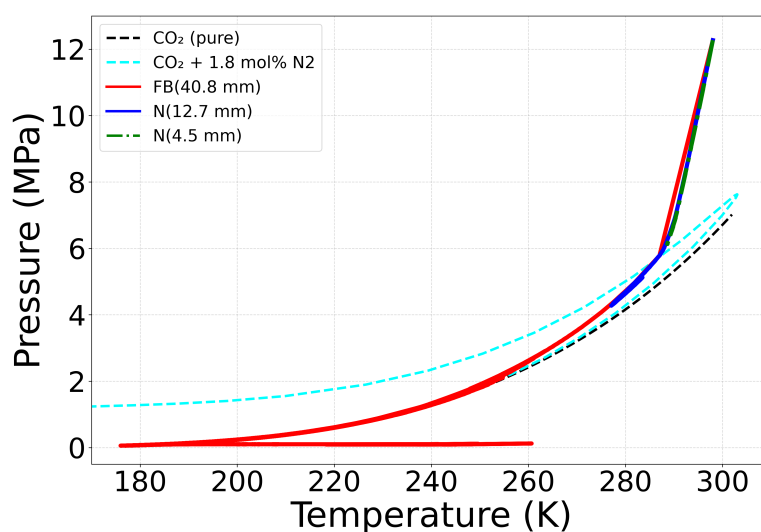


Figure 8. Cont.

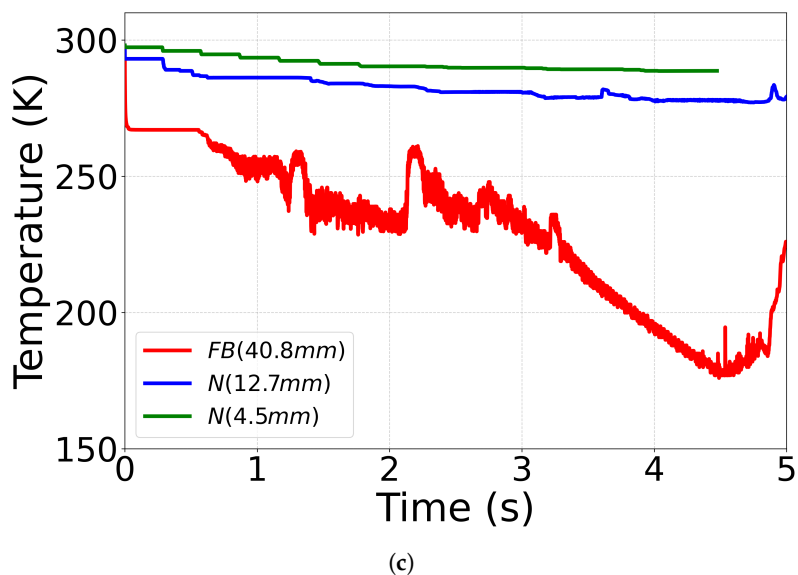


Figure 8. (a) Thermodynamic path for different outlet diameter and nozzle geometry. (b) Pressure and gas fraction comparison for different outlet diameter and nozzle geometry. Dark lines represent pressure while light lines represent gas fraction profiles. (c) Temperature profiles for different outlet diameter and nozzle geometry. Outlet type abbreviations: FB — Full Bore; N — Nozzle.

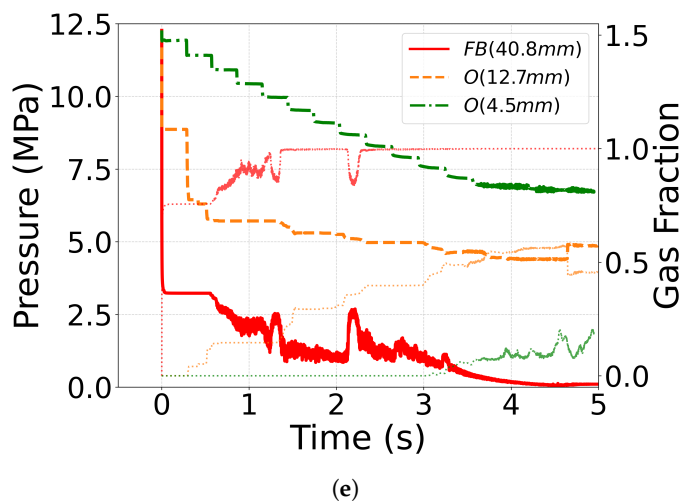
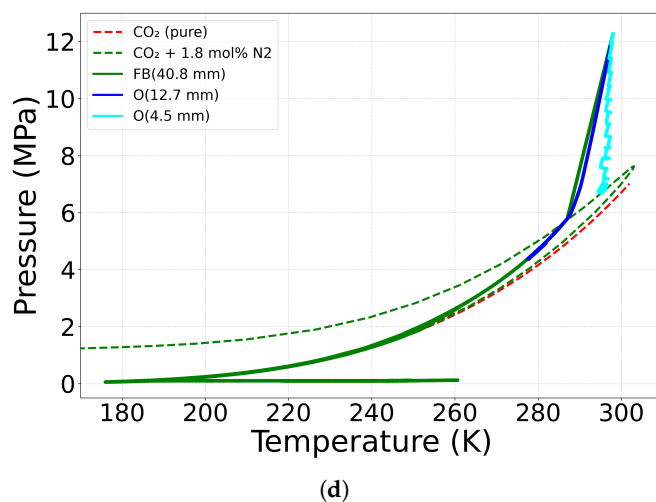


Figure 9. *Cont.*

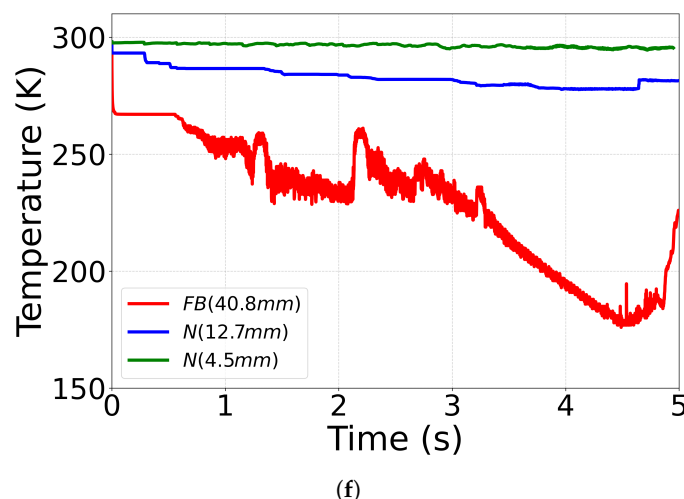
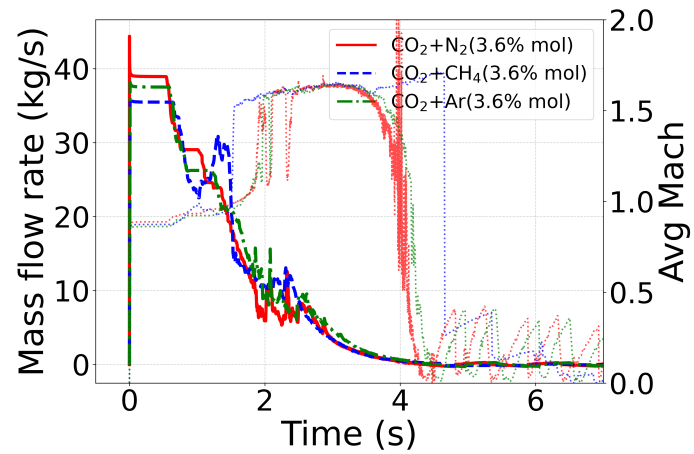


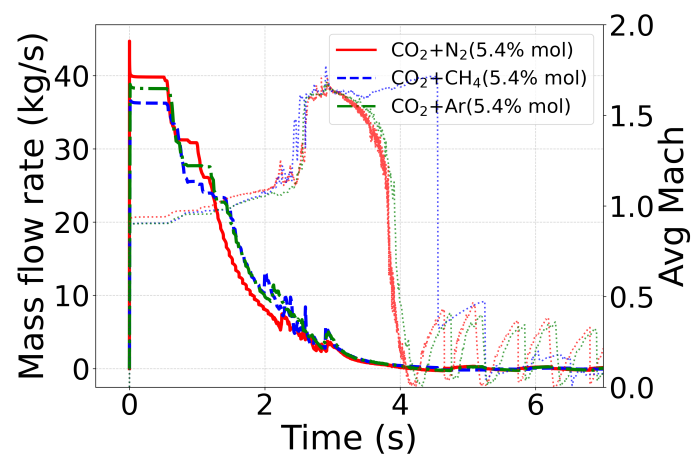
Figure 9. (a) Thermodynamic path for different outlet diameter and orifice geometry. (b) Pressure and gas fraction comparison for different outlet diameter and orifice geometry. Dark lines represent pressure while light lines represent gas fraction profiles (c) Temperature profiles for different outlet diameter and orifice geometry. Outlet type abbreviations: FB — Full Bore; O — Orifice.

4.5. Mass-Flow Rate and Mach Number

The primary objective of this work is to develop a database of mass flow rate, pressure, and gas-phase properties that can serve as inputs for dispersion models predicting the spread of CO_2 mixtures during pressure leakage events. In current industrial practice, discharge predictions largely rely on steady or quasi-steady formulations and empirical choked-flow correlations. These approaches depend strongly on the mixture speed of sound and its variation during phase change. Therefore, the present study reports both mass flow rate and Mach number for comparison. All reported quantities in Figure 10 correspond to mass-averaged values evaluated at the rupture/outflow plane. Density and velocity are coupled to each other, variation is always in both to maintain continuity. Initially the density is higher representing the presence of liquid, then reducing to air density. Accordingly the velocity varies, the variation in pressure, temperature in previous plots and mass fraction in Figure 10 and Figure 11 represent the sudden change in gas-fraction caused during two instances of the simulation: when released from the choked flow state and when phase changes from two-phase to gas phase. The initial choked flow condition is the duration at which the fluid exits at the maximum mass flow rate. This maximum mass flow rate for each impurity is found to be less dependent on mixture composition (i.e. mol % 3.6-5.4) and majorly the function of initial (supercritical) and outflow conditions only. However, in comparison of the different impurities this maximum mass flow rate decreases as $\text{N}_2 > \text{Ar} > \text{CH}_4$. The flow enters the two-phase state at sub-sonic conditions but close to Mach 1 (i.e. $M_{en} \simeq 0.8$), while close to the gaseous state the fluid Mach number rises rapidly to balance the decrease in density and maintain the continuity. The maximum Mach number is found to be close to 1.7 (i.e. $M_{out} \simeq 1.7$), and is attained in the two-phase region before to transition to the gaseous phase where the Mach number decreases abruptly due to the higher speed of sound in the gaseous state. Similarly, Figure 11 reports the mass flow rate and mach number for various outlet diameter and geometries in the present study. The mass flow rate for the nozzle is found to be closer to the experimental data, but not for the orifice. This could be because of the sharp change in flow field for the case of orifice in comparison to the nozzle. The effect of vena-contracta and coefficient of discharge is severe for the case of orifice and need to be considered and modeled more accurately.

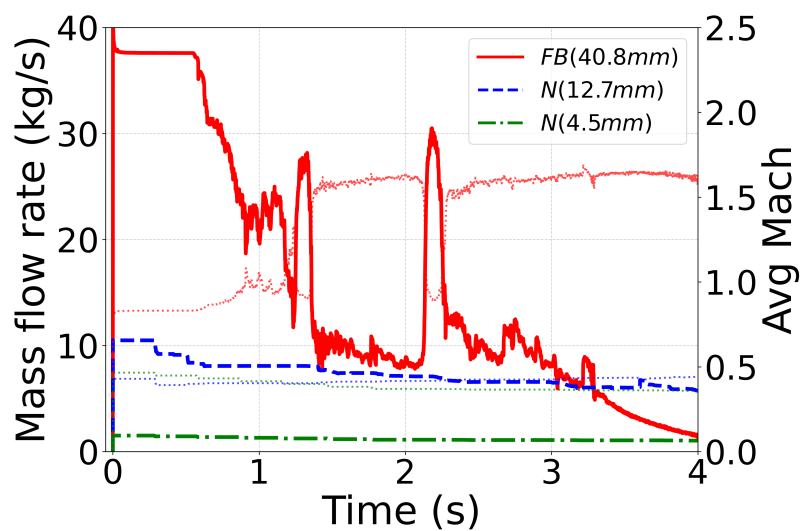


(g)



(h)

Figure 10. (a) Mass flow rate and Mach number comparison for various CO_2 mixtures for the composition of 3.6% by mol. (b) Mass flow rate and Mach number comparison for various CO_2 mixtures for the composition of 5.4% by mol.



(a)

Figure 11. Cont.

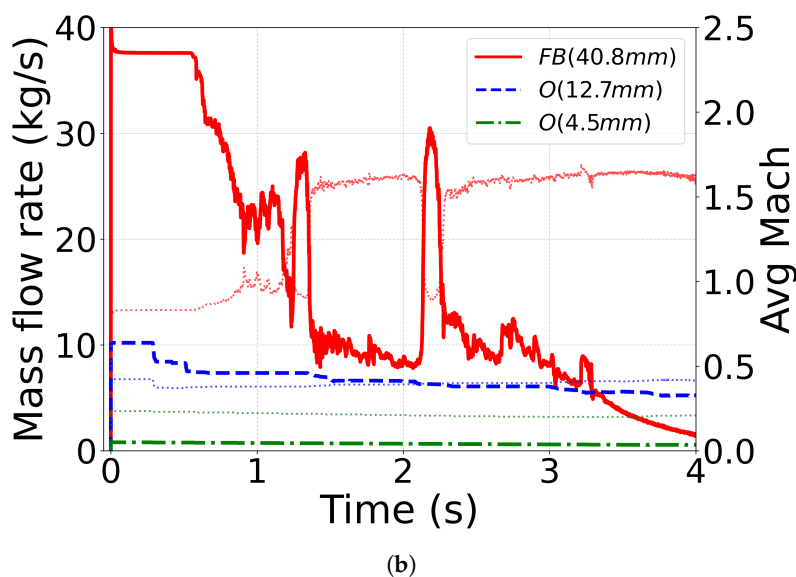


Figure 11. (a) Mass flow rate and Mach number comparison for $\text{CO}_2 + \text{N}_2$ mixture for various nozzle diameters. (b) Mass flow rate and Mach number comparison for $\text{CO}_2 + \text{N}_2$ mixture for various orifice diameters.

5. $s\text{CO}_2$ Pipeline Transport: Industrial Scale Simulation

For real life applications, the pipeline transport expands to the order of km instead of m. For such configuration, a 50km long pipeline depressurization case has been studied in [84]. A simulation of this scale generates increased complexity, particularly in terms of computational costs. Wall heat transfer model, pressure loss along the pipeline, venting tubes, turbulence, gravity effects cannot be neglected anymore.

5.1. Setup of the 50km Pipeline with Venting

A rectangular geometry is chosen instead of a circular cylinder for simplicity for the case of 50km long pipe depressurization, indeed keeping the effective area identical to the actual circular pipeline. From few preliminary simulations, it is observed that the venting configuration plays a significant role in the depressurization dynamics, as the venting pipe diameter ($d = 7$ inch) is substantially smaller than the main pipeline diameter ($d = 24$ inch). This pronounced area contraction governs the discharge characteristics and strongly influences the pressure decay rate. Therefore, two different venting configurations i.e. horizontal and vertical venting have been investigated taking advantage of the 3D-based finite volume method used in this work. A detailed description of both configurations are shown in Figure 12. The boundary conditions are similar to the previous short pipelines setup, i.e. Dirichlet for pressure at the outlet, isothermal wall and no slip condition at the rest of the wall. Boundary conditions along-with initial condition are also shown in Figure 12.

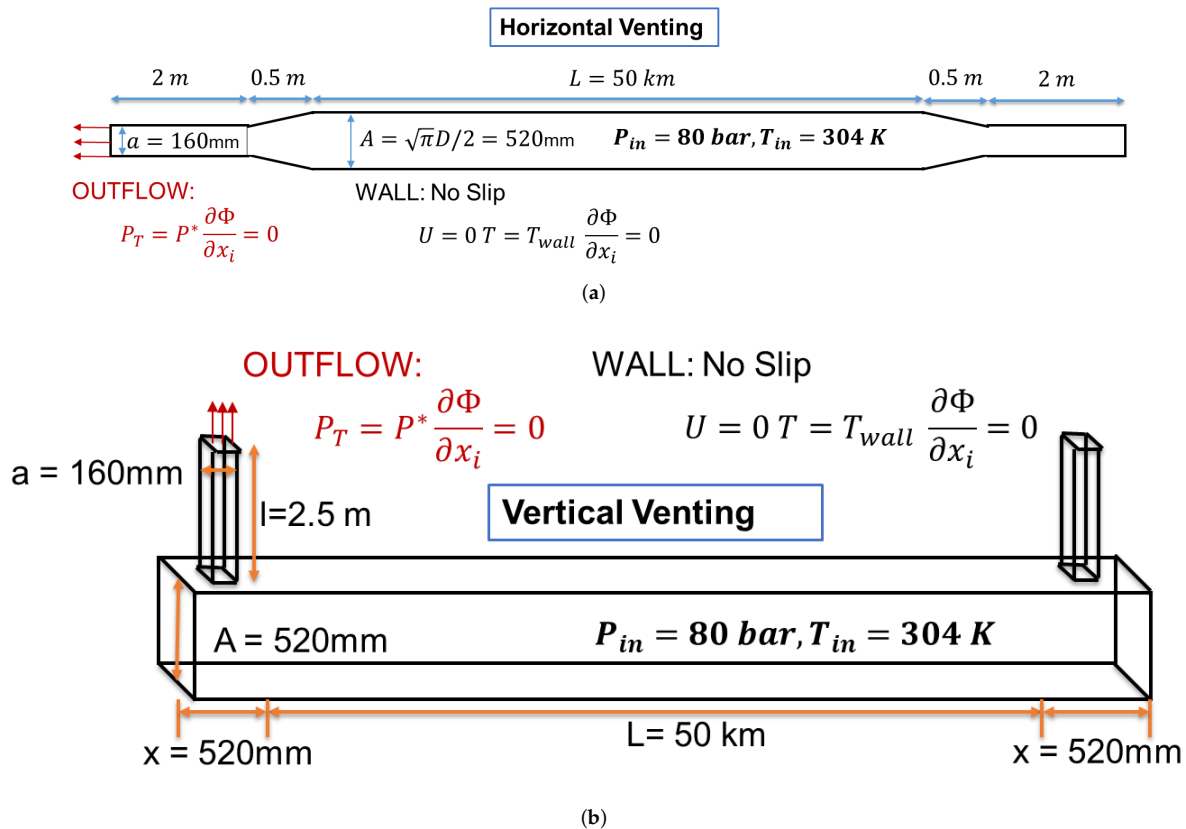


Figure 12. (a) Horizontal venting configuration setup. (b) Vertical venting configuration setup.

5.2. Pressure and Temperature Profiles

It can be seen from Figure 13(a) and Figure 13(b) that the vertical venting configuration outperforms the horizontal one to great extent, implying not only that the venting area is important but also the role of gravity for such configuration. The pressure profiles tend to follow the similar trend as the experimental for both the configurations, with vertical venting being more close to the experimental data. Some deviations begin when the simulation is close to 2 hours in physical time scale, as the effects of heat transfer and pipe loss are expected to be predominant after such long duration. Hence, the future work is to analyze the problem with a coupled conjugate heat transfer model along with skeletal pipeline configuration. The horizontal venting configuration requires approximately 2 days of wall-clock time on 256 cores to simulate 2 hours of physical time. In contrast, the vertical venting configuration requires nearly 8 days under identical computational resources and simulation duration. The extended computational time is primarily due to the severe time-step restriction imposed by the physics of the problem. The allowable time step is limited by stability constraints, which are directly linked to the smallest cell volume in the domain. Larger time steps would require larger cell volumes; however, this is not feasible in the present case. In the vertical venting configuration, resolving gravity-driven stratification and slip effects in the venting section requires to maintain a minimum of 10 cells along the vertical direction. This refinement significantly reduces the minimum cell volume in the domain, thereby imposing a much smaller stable time step and consequently increasing the total computational time.

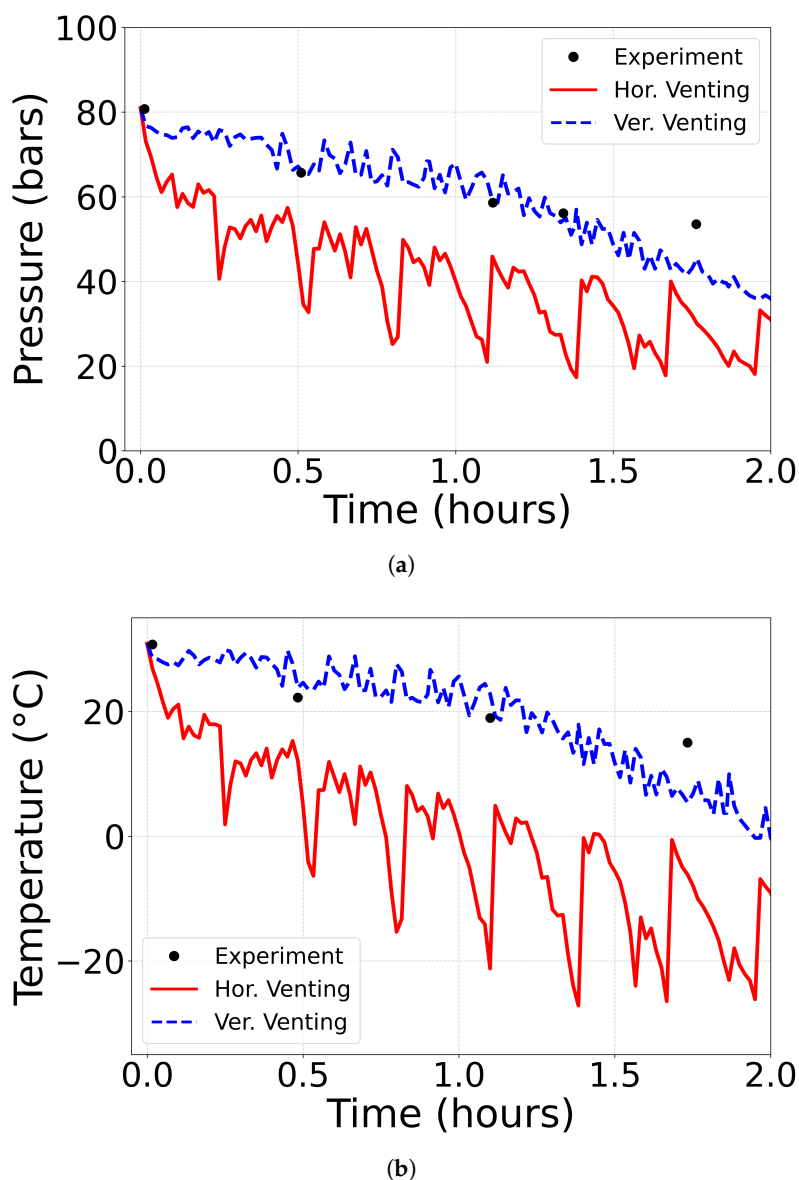


Figure 13. (a) Pressure and (b) Temperature comparison for different venting configuration and experiment [84] for 50 km long pipe depressurization.

6. Conclusions

The present work shows that the real-fluid (RFM) equilibrium framework is capable to model supercritical CO_2 pipeline transport problems with good accuracy. A good match was found between simulation results and experimental data. First, the isothermal heat transfer model and the CPA-EoS have been proven to be best suitable for sCO_2 fluid simulations. Next, the role of impurities has been investigated. Although the impurities not only shift thermodynamic boundaries but also alter the kinetics of phase transitions, it is revealed that the amount of impurities is less predominant near the critical condition operations, as the depressurization rate, wave speed and pressure profiles are found to be similar. Besides, the outlet geometry tends to impact the thermodynamic path to a great extent. It is found that for the nozzle geometries where there is a smooth change in the cross-section area, the simulation predictions were quite close to the experiment. However, for the case of the orifices where there is a sharp change in the cross-section area, the simulation under predict the leakage mass flow rate, implying a necessary computationally refined discretization for the outlet geometry. Finally, the role of venting area and gravity is found to be predominant for the 50km sCO_2 pipeline depressurization, to capture the initial physics of depressurization. The conjugate heat transfer (CHT)

model and modeling of losses in pipes at the wall level become essential for subsequent stages when considering buried pipelines.

Author Contributions: Conceptualization, methodology, and formal analysis, K.K., C.H., M.H., H.A., and J-C.d.H.; software, K.K., M.H. and H.A.; validation and investigation, K.K.; resources, C.H.; data curation, K.K.; writing—original draft preparation, K.K.; writing—review and editing, C.H., M.H., H.A., and J-C.d.H.; supervision, C.H. and J-C.d.H.; project administration, C.H.; funding acquisition, C.H. All authors have read and agreed to the published version of the manuscript.

Funding: This research received no external funding.

Institutional Review Board Statement: Not applicable.

Informed Consent Statement: Not applicable.

Data Availability Statement: Data available on request due to restrictions.

Acknowledgments: K.K. would like to acknowledge ANR support for providing the financial support.

Conflicts of Interest: The author(s) declare no potential conflicts of interest with respect to the research, authorship, and/or publication of this article.

Abbreviations

The following abbreviations are used in this manuscript:

CCUS	Carbon Capture and Storage
RFM	Real Fluid Method
sCO ₂	Supercritical CO ₂
VLE	Vapor Liquid Equilibrium
EoS	Equation of State
PR	Peng Robinson
CPA	Cubic Plus Association
SAFT	Perturbed-Chain Statistical Associating Fluid Theory
M_{en}	Mass flow rate at the transition from dense phase to two-phase
M_{out}	Mass flow rate at the transition from two-phase to gaseous phase

References

1. Eide, L.I.; Batum, M.; Dixon, T.; Elamin, Z.; Graue, A.; Hagen, S.; Hovorka, S.; Nazarian, B.; Nøkleby, P.H.; Olsen, G.I.; et al. Enabling large-scale carbon capture, utilisation, and storage (CCUS) using offshore carbon dioxide (CO₂) infrastructure developments—a review. *Energies* **2019**, *12*, 1945.
2. Rui, Z.; Zeng, L.; Dindoruk, B. Challenges in the large-scale deployment of CCUS. *Engineering* **2025**, *44*, 17–20.
3. Boot-Handford, M.E.; Abanades, J.C.; Anthony, E.J.; Blunt, M.J.; Brandani, S.; Mac Dowell, N.; Fernández, J.R.; Ferrari, M.C.; Gross, R.; Hallett, J.P.; et al. Carbon capture and storage update. *Energy & Environmental Science* **2014**, *7*, 130–189.
4. Leung, D.Y.; Caramanna, G.; Maroto-Valer, M.M. An overview of current status of carbon dioxide capture and storage technologies. *Renewable and sustainable energy reviews* **2014**, *39*, 426–443.
5. Haszeldine, R.S. Carbon capture and storage: how green can black be? *Science* **2009**, *325*, 1647–1652.
6. Wareing, C.J.; Fairweather, M.; Falle, S.A.; Woolley, R.M. Modelling ruptures of buried high pressure dense phase CO₂ pipelines in carbon capture and storage applications—Part I. Validation. *International Journal of Greenhouse Gas Control* **2015**, *42*, 701–711.
7. Martynov, S.; Zheng, W.; Mahgerfteh, H.; Brown, S.; Hebrard, J.; Jamois, D.; Proust, C. Computational and experimental study of solid-phase formation during the decompression of high-pressure CO₂ pipelines. *Industrial & Engineering Chemistry Research* **2018**, *57*, 7054–7063.
8. Brown, S.; Martynov, S.; Mahgerfteh, H.; Chen, S.; Zhang, Y. Modelling the non-equilibrium two-phase flow during depressurisation of CO₂ pipelines. *International Journal of Greenhouse Gas Control* **2014**, *30*, 9–18.
9. Peletiri, S.P.; Rahmanian, N.; Mujtaba, I.M. CO₂ Pipeline design: A review. *Energies* **2018**, *11*, 2184.

10. Bielka, P.; Kuczyński, S.; Włodek, T.; Nagy, S. Risks and safety of CO₂ pipeline transport: a case study of the analysis and modeling of the risk of accidental release of CO₂ into the atmosphere. *Energies* **2024**, *17*, 3943.
11. Lu, H.; Ma, X.; Huang, K.; Fu, L.; Azimi, M. Carbon dioxide transport via pipelines: A systematic review. *Journal of Cleaner Production* **2020**, *266*, 121994.
12. Mahgerefteh, H.; Brown, S.; Martynov, S. A study of the effects of friction, heat transfer, and stream impurities on the decompression behavior in CO₂ pipelines. *Greenhouse gases: science and technology* **2012**, *2*, 369–379.
13. Woolley, R.M.; Fairweather, M.; Wareing, C.J.; Falle, S.A.; Mahgerefteh, H.; Martynov, S.; Brown, S.; Narasimhamurthy, V.D.; Storvik, I.E.; Saelen, L.; et al. CO₂PipeHaz: quantitative hazard assessment for next generation CO₂ pipelines. *Energy Procedia* **2014**, *63*, 2510–2529.
14. Wareing, C.J.; Fairweather, M.; Woolley, R.M.; Falle, S.A. Numerical simulation of CO₂ dispersion from punctures and ruptures of buried high-pressure dense phase CO₂ pipelines with experimental validation. *Energy Procedia* **2014**, *63*, 2500–2509.
15. Pham, L.H.H.P.; Rusli, R. A review of experimental and modelling methods for accidental release behaviour of high-pressurised CO₂ pipelines at atmospheric environment. *Process Safety and Environmental Protection* **2016**, *104*, 48–84.
16. Munkejord, S.T.; Hammer, M.; Løvseth, S.W. CO₂ transport: Data and models—A review. *Applied Energy* **2016**, *169*, 499–523.
17. Vitali, M.; Corvaro, F.; Marchetti, B.; Terenzi, A. Thermodynamic challenges for CO₂ pipelines design: A critical review on the effects of impurities, water content, and low temperature. *International Journal of Greenhouse Gas Control* **2022**, *114*, 103605.
18. Shang, Y.; Chen, X.; Yang, M.; Xing, X.; Jiao, J.; An, G.; Li, X.; Xiong, X. Comprehensive review on leakage characteristics and diffusion laws of carbon dioxide pipelines. *Energy & Fuels* **2024**, *38*, 10456–10493.
19. Gu, S.; Li, Y.; Teng, L.; Hu, Q.; Zhang, D.; Ye, X.; Wang, C.; Wang, J.; Iglauer, S. A new model for predicting the decompression behavior of CO₂ mixtures in various phases. *Process Safety and Environmental Protection* **2018**, *120*, 237–247.
20. Magen, O.; Kozak, Y.; Di Lucchio, L.; Marengo, M.; Bar-Kohany, T. Predicting nucleation pressure under rapid depressurization: Bridging positive and negative pressure regions. *International Journal of Heat and Mass Transfer* **2025**, *251*, 127309.
21. He, X.; Gao, P.; Wang, J.; Zhang, Z. Experimental investigation on hot water rapid depressurization process characteristics inside and outside of the ruptured pipeline. *Nuclear Engineering and Design* **2024**, *425*, 113341.
22. Liao, H.; Wang, X.; Yang, K.; Hou, Z.; Wang, H. Impurity-driven variations in CO₂ critical flow dynamics: Modeling approaches for enhanced CCS safety. *Energy* **2025**, *323*, 135850.
23. Cao, Q.; Yan, X.; Liu, S.; Yu, J.; Chen, S.; Zhang, Y. Temperature and phase evolution and density distribution in cross section and sound evolution during the release of dense CO₂ from a large-scale pipeline. *International Journal of Greenhouse Gas Control* **2020**, *96*, 103011.
24. Hansen, P.M.; Gaathaug, A.V.; Bjerketvedt, D.; Vaagsaether, K. The behavior of pressurized liquefied CO₂ in a vertical tube after venting through the top. *International Journal of Heat and Mass Transfer* **2017**, *108*, 2011–2020.
25. Hansen, P.M.; Gaathaug, A.V.; Bjerketvedt, D.; Vaagsaether, K. Rapid depressurization and phase transition of CO₂ in vertical ducts—small-scale experiments and Rankine-Hugoniot analyses. *Journal of Hazardous Materials* **2019**, *365*, 16–25.
26. Bhuvankar, P.; Cihan, A.; Birkholzer, J. A framework to simulate the blowout of CO₂ through wells in geologic carbon storage. *International Journal of Greenhouse Gas Control* **2023**, *127*, 103921.
27. Yin, B.; Huang, W.; Ouyang, X.; Zhao, X.; Meng, L.; Zhang, L.; Hu, Q.; Li, Y. A transient model considering non-equilibrium phase transition in CO₂ pipe decompression. *Journal of Pipeline Science and Engineering* **2025**, p. 100324.
28. Log, A.M.; Hammer, M.; Deng, H.; Austegard, A.; Hafner, A.; Munkejord, S.T. Depressurization of CO₂ in a pipe: Effect of initial state on non-equilibrium two-phase flow. *International Journal of Multiphase Flow* **2024**, *170*, 104624.
29. Wang, J.; Lu, Z.; Wu, S.; Zhang, Z.; Liu, J. Research on non-equilibrium characteristics and relaxation time parameter optimization in high-pressure CO₂ pipeline depressurization. *International Communications in Heat and Mass Transfer* **2025**, *169*, 109527.
30. Log, A.M.; Hammer, M.; Munkejord, S.T. A flashing flow model for the rapid depressurization of CO₂ in a pipe accounting for bubble nucleation and growth. *International Journal of Multiphase Flow* **2024**, *171*, 104666.

31. Munkejord, S.T.; Deng, H.; Austegard, A.; Hammer, M.; Aasen, A.; Skarsvåg, H.L. Depressurization of CO₂-N₂ and CO₂-He in a pipe: Experiments and modelling of pressure and temperature dynamics. *International Journal of Greenhouse Gas Control* **2021**, *109*, 103361.
32. Yu, S.; Yan, X.; He, Y.; Chen, L.; Hu, Y.; Yang, K.; Cao, Z.; Yu, J.; Chen, S. Study on the decompression behavior during large-scale pipeline puncture releases of CO₂ with various N₂ compositions: Experiments and mechanism analysis. *Energy* **2024**, *296*, 131180.
33. Zhu, J.; Wu, J.; Xie, N.; Li, Z.; Hu, Q.; Li, Y. Study on water hammer phase transition characteristics of dense/liquid phase CO₂ pipeline. *Energy* **2024**, *311*, 133470.
34. Liao, H.; Yang, K.; Liang, Z.; Hu, H.; Wang, X.; Wang, H. A new paradigm in critical flow analysis: Combining Buckingham Pi theorem with neural network for improved predictions in microchannels. *Chemical Engineering Science* **2024**, *299*, 120483.
35. Yu, S.; Yan, X.; He, Y.; Hu, Y.; Qiao, F.; Yang, K.; Cao, Z.; Chen, L.; Liu, Z.; Yu, J.; et al. Study on the effect of valve openings and multi-stage throttling structures on the pressure and temperature during CO₂ pipeline venting processes. *Energy* **2024**, *308*, 132967.
36. Ding, Y.; Xu, P.; Lu, Y.; Yang, M.; Zhang, J.; Liu, K. Research on pipeline leakage calculation and correction method based on numerical calculation method. *Energies* **2023**, *16*, 7255.
37. Zhang, Z.; Lu, Z.; Yan, L.; Wang, J.; Yao, S. Experiment and numerical investigation on flow characteristics and near-field structure of dense phase CO₂ pipeline leakage. *Process Safety and Environmental Protection* **2024**, *182*, 327–344.
38. Yu, S.; Yan, X.; He, Y.; Yu, J.; Chen, S. Study on the leakage morphology and temperature variations in the soil zone during large-scale buried CO₂ pipeline leakage. *Energy* **2024**, *288*, 129674.
39. Shang, Y.; Xing, X.; Chen, X.; Yang, M.; Shah, R.K.; Pang, X. Developing Transient Model and Simulating the Effects of Soil Properties on a Small Hole Leakage and Diffusion Characteristics in the Buried CO₂ Pipelines. *Energy & Fuels* **2025**.
40. Chen, L.; Yan, X.; Hu, Y.; Yang, K.; Yu, S.; Yu, J.; Chen, S. Depressurization and heat transfer during leakage of supercritical CO₂ from a pipeline. *Greenhouse Gases: Science and Technology* **2022**, *12*, 616–628.
41. Hu, Y.; Han, H.; Jing, R.; Hu, Q.; Li, Y. Experimental analysis of pressure response and jet behavior in underwater supercritical CO₂ pipeline leakage. *Ocean Engineering* **2025**, *341*, 122469.
42. Span, R.; Wagner, W. A new equation of state for carbon dioxide covering the fluid region from the triple-point temperature to 1100 K at pressures up to 800 MPa. *Journal of physical and chemical reference data* **1996**, *25*, 1509–1596.
43. Nazeri, M.; Chapoy, A.; Burgass, R.; Tohidi, B. Measured densities and derived thermodynamic properties of CO₂-rich mixtures in gas, liquid and supercritical phases from 273 K to 423 K and pressures up to 126 MPa. *The Journal of Chemical Thermodynamics* **2017**, *111*, 157–172.
44. Demetriades, T.A.; Graham, R.S. A new equation of state for CCS pipeline transport: Calibration of mixing rules for binary mixtures of CO₂ with N₂, O₂ and H₂. *The Journal of Chemical Thermodynamics* **2016**, *93*, 294–304.
45. Kunz, O.; Wagner, W. The GERG-2008 wide-range equation of state for natural gases and other mixtures: An expansion of GERG-2004. *Journal of chemical & engineering data* **2012**, *57*, 3032–3091.
46. Petropoulou, E.; Voutsas, E.; Westman, S.F.; Austegard, A.; Stang, H.G.J.; Løvseth, S.W. Vapor-liquid equilibrium of the carbon dioxide/methane mixture at three isotherms. *Fluid Phase Equilibria* **2018**, *462*, 44–58.
47. Li, H.; Yan, J. Evaluating cubic equations of state for calculation of vapor–liquid equilibrium of CO₂ and CO₂-mixtures for CO₂ capture and storage processes. *Applied Energy* **2009**, *86*, 826–836.
48. Diamantonis, N.I.; Boulougouris, G.C.; Mansoor, E.; Tsangaris, D.M.; Economou, I.G. Evaluation of cubic, SAFT, and PC-SAFT equations of state for the vapor–liquid equilibrium modeling of CO₂ mixtures with other gases. *Industrial & Engineering Chemistry Research* **2013**, *52*, 3933–3942.
49. Gross, J.; Sadowski, G. Perturbed-chain SAFT: An equation of state based on a perturbation theory for chain molecules. *Industrial & engineering chemistry research* **2001**, *40*, 1244–1260.
50. Avendano, C.; Lafitte, T.; Galindo, A.; Adjiman, C.S.; Jackson, G.; Müller, E.A. SAFT- γ force field for the simulation of molecular fluids. 1. A single-site coarse grained model of carbon dioxide. *The Journal of Physical Chemistry B* **2011**, *115*, 11154–11169.
51. Lymperiadis, A.; Adjiman, C.S.; Galindo, A.; Jackson, G. A group contribution method for associating chain molecules based on the statistical associating fluid theory (SAFT- γ). *The Journal of chemical physics* **2007**, *127*.

52. Bahadori, A.; Vuthaluru, H.B. Predictive tool for an accurate estimation of carbon dioxide transport properties. *International Journal of Greenhouse Gas Control* **2010**, *4*, 532–536.
53. Nazeri, M.; Chapoy, A.; Valtz, A.; Coquelet, C.; Tohidi, B. New experimental density data and derived thermophysical properties of carbon dioxide–Sulphur dioxide binary mixture (CO₂–SO₂) in gas, liquid and supercritical phases from 273 K to 353 K and at pressures up to 42 MPa. *Fluid Phase Equilibria* **2017**, *454*, 64–77.
54. Jarraghan, A.; Heidaryan, E. A novel correlation approach to estimate thermal conductivity of pure carbon dioxide in the supercritical region. *The Journal of Supercritical Fluids* **2012**, *64*, 39–45.
55. Rostami, A.; Arabloo, M.; Ebadi, H. Genetic programming (GP) approach for prediction of supercritical CO₂ thermal conductivity. *Chemical Engineering Research and Design* **2017**, *122*, 164–175.
56. Hellmann, R.; Bich, E.; Vesovic, V. Cross second virial coefficients and dilute gas transport properties of the (CH₄+ CO₂), (CH₄+ H₂S), and (H₂S+ CO₂) systems from accurate intermolecular potential energy surfaces. *The Journal of Chemical Thermodynamics* **2016**, *102*, 429–441.
57. Li, H.; Wilhelmsen, Ø.; Lv, Y.; Wang, W.; Yan, J. Viscosities, thermal conductivities and diffusion coefficients of CO₂ mixtures: Review of experimental data and theoretical models. *International Journal of Greenhouse Gas Control* **2011**, *5*, 1119–1139.
58. Martin Trusler, J. Equation of state for solid phase I of carbon dioxide valid for temperatures up to 800 K and pressures up to 12 GPa. *Journal of Physical and Chemical Reference Data* **2011**, *40*.
59. Martin Trusler, J. Erratum: Equation of state for solid phase I of carbon dioxide valid for temperatures up to 800 K and pressures up to 12 GPa [J. Phys. Chem. Ref. Data *40*, 043105 (2011)]. *Journal of Physical and Chemical Reference Data* **2012**, *41*, 039901.
60. Jäger, A.; Span, R. Equation of state for solid carbon dioxide based on the Gibbs free energy. *Journal of Chemical & Engineering Data* **2012**, *57*, 590–597.
61. Nikolaidis, I.K.; Boulougouris, G.C.; Peristeras, L.D.; Economou, I.G. Equation-of-State Modeling of Solid–Liquid–Gas Equilibrium of CO₂ Binary Mixtures. *Industrial & engineering chemistry research* **2016**, *55*, 6213–6226.
62. Løvseth, S.W.; Austegard, A.; Westman, S.F.; Stang, H.G.J.; Herrig, S.; Neumann, T.; Span, R. Thermodynamics of the carbon dioxide plus argon (CO₂+ ar) system: An improved reference mixture model and measurements of vapor-liquid, vapor-solid, liquid-solid and vapor-liquid-solid phase equilibrium data at the temperatures 213–299 K and pressures up to 16 MPa. *Fluid Phase Equilibria* **2018**, *466*, 48–78.
63. Tang, L.; Li, C.; Lim, S. Solid–liquid–vapor equilibrium model applied for a CH₄–CO₂ binary mixture. *Industrial & Engineering Chemistry Research* **2019**, *58*, 18355–18366.
64. Maltby, T.W.; Aasen, A.; Hammer, M.; Wilhelmsen, Ø. Review of Experimental Data and Evaluation of Equations of State for Modeling Formation of Solid CO₂ in CCS and Natural Gas Applications. *Industrial & Engineering Chemistry Research* **2025**.
65. Bhatia, H.; Habchi, C. Real Fluid Modeling and Simulation of the Structures and Dynamics of Condensation in CO₂ Flows Shocked Inside a de Laval Nozzle, Considering the Effects of Impurities. *Applied Sciences* **2023**, *13*, 10863.
66. Yang, S.; Yi, P.; Habchi, C. Real-fluid injection modeling and LES simulation of the ECN Spray A injector using a fully compressible two-phase flow approach. *International Journal of Multiphase Flow* **2020**, *122*, 103145.
67. Yi, P.; Yang, S.; Habchi, C.; Lugo, R. A multicomponent real-fluid fully compressible four-equation model for two-phase flow with phase change. *Physics of Fluids* **2019**, *31*.
68. Gaballa, H.; Jafari, S.; Habchi, C.; de Hemptinne, J.C. Numerical investigation of droplet evaporation in high-pressure dual-fuel conditions using a tabulated real-fluid model. *International Journal of Heat and Mass Transfer* **2022**, *189*, 122671.
69. de Hemptinne, J.C.; Ferrando, N.; Hajiw-Riberaud, M.; Lachet, V.; Maghsoodloo, S.; Mougin, P.; Ngo, T.D.; Pigeon, L.; Yanes, J.R.; Wender, A. Carnot: a thermodynamic library for energy industries. *Science and Technology for Energy Transition* **2023**, *78*, 30.
70. Munkejord, S.T.; Austegard, A.; Deng, H.; Hammer, M.; Stang, H.J.; Løvseth, S.W. Depressurization of CO₂ in a pipe: High-resolution pressure and temperature data and comparison with model predictions. *Energy* **2020**, *211*, 118560.
71. Hammer, M.; Deng, H.; Austegard, A.; Log, A.M.; Munkejord, S.T. Experiments and modelling of choked flow of CO₂ in orifices and nozzles. *International Journal of Multiphase Flow* **2022**, *156*, 104201.
72. GRTgaz S.A.. Proposition de spécifications dioxyde de carbone. Technical report, GRTgaz S.A., 2023. Technical report.

73. Habchi, C.; Gaballa, H.; de Hemptinne, J.C. A new real-fluid modelling framework applied to cavitation simulation. In Proceedings of the 12th International Cavitation – CAV2024, 2-7 June, CHANIA, GREECE, 2024.
74. Jafari, S.; Gaballa, H.; Habchi, C.; de Hemptinne, J.C. Towards understanding the structure of subcritical and transcritical liquid–gas interfaces using a tabulated real fluid modeling approach. *Energies* **2021**, *14*, 5621.
75. Jafari, S.; Gaballa, H.; Habchi, C.; De Hemptinne, J.C.; Mougin, P. Exploring the interaction between phase separation and turbulent fluid dynamics in multi-species supercritical jets using a tabulated real-fluid model. *The Journal of Supercritical Fluids* **2022**, *184*, 105557.
76. Gaballa, H.; Habchi, C.; de Hemptinne, J.C. Modeling and LES of high-pressure liquid injection under evaporating and non-evaporating conditions by a real fluid model and surface density approach. *International Journal of Multiphase Flow* **2023**, *160*, 104372.
77. Chung, T.H.; Ajlan, M.; Lee, L.L.; Starling, K.E. Generalized multiparameter correlation for nonpolar and polar fluid transport properties. *Industrial & engineering chemistry research* **1988**, *27*, 671–679.
78. Nicoud, F.; Toda, H.B.; Cabrit, O.; Bose, S.; Lee, J. Using singular values to build a subgrid-scale model for large eddy simulations. *Physics of fluids* **2011**, *23*.
79. Peng, D.Y.; Robinson, D.B. A new two-constant equation of state. *Industrial & Engineering Chemistry Fundamentals* **1976**, *15*, 59–64.
80. Kontogeorgis, G.M.; Voutsas, E.C.; Yakoumis, I.V.; Tassios, D.P. An equation of state for associating fluids. *Industrial & engineering chemistry research* **1996**, *35*, 4310–4318.
81. Ware, C.; Knight, W.; Wells, D. Memory intensive statistical algorithms for multibeam bathymetric data. *Computers & Geosciences* **1991**, *17*, 985–993.
82. Gaballa, H.; Jafari, S.; Di-Lella, A.; Habchi, C.; et al. A tabulated real-fluid modeling approach applied to renewable dual-fuel evaporation and mixing: Paper 216. In Proceedings of the International Conference on Liquid Atomization and Spray Systems (ICLASS), 2021, Vol. 1.
83. Senecal, P.; Pomraning, E.; Richards, K.; Som, S. Grid-convergent spray models for internal combustion engine computational fluid dynamics simulations. *Journal of Energy Resources Technology* **2014**, *136*, 012204.
84. Clausen, S.; Oosterkamp, A.; Strøm, K.L. Depressurization of a 50 km long 24 inches CO₂ pipeline. *Energy Procedia* **2012**, *23*, 256–265.

Disclaimer/Publisher’s Note: The statements, opinions and data contained in all publications are solely those of the individual author(s) and contributor(s) and not of MDPI and/or the editor(s). MDPI and/or the editor(s) disclaim responsibility for any injury to people or property resulting from any ideas, methods, instructions or products referred to in the content.